

RESEARCH ARTICLE

The critical balance between dopamine D2 receptor and RGS for the sensitive detection of a transient decay in dopamine signal

Hidetoshi Urakubo^{1,2*}, Sho Yagishita^{3,4}, Haruo Kasai^{3,4}, Yoshiyuki Kubota^{2,5}, Shin Ishii^{1,4}

1 Integrated Systems Biology Laboratory, Department of Systems Science, Graduate School of Informatics, Kyoto University, Kyoto, Japan, **2** Section of Electron Microscopy, National Institute for Physiological Sciences, Okazaki, Aichi, Japan, **3** Laboratory of Structural Physiology, Center for Disease Biology and Integrative Medicine, Faculty of Medicine, University of Tokyo, Bunkyo-ku, Tokyo, Japan, **4** International Research Center for Neurointelligence (WPI-IRCN), University of Tokyo Institutes for Advanced Study (UTIAS), Tokyo, Japan, **5** Department of Physiological Sciences, The Graduate University for Advanced Studies (SOKENDAI), Okazaki, Aichi, Japan

* hurakubo@gmail.com

OPEN ACCESS

Citation: Urakubo H, Yagishita S, Kasai H, Kubota Y, Ishii S (2021) The critical balance between dopamine D2 receptor and RGS for the sensitive detection of a transient decay in dopamine signal. *PLoS Comput Biol* 17(9): e1009364. <https://doi.org/10.1371/journal.pcbi.1009364>

Editor: Joanna Jędrzejewska-Szmek, Instytut Biologii Doświadczalnej im M Nenckiego Polskiej Akademii Nauk, POLAND

Received: December 15, 2020

Accepted: August 18, 2021

Published: September 30, 2021

Copyright: © 2021 Urakubo et al. This is an open access article distributed under the terms of the [Creative Commons Attribution License](https://creativecommons.org/licenses/by/4.0/), which permits unrestricted use, distribution, and reproduction in any medium, provided the original author and source are credited.

Data Availability Statement: Developed MATLAB code is available at the public repository GitHub (<https://github.com/urakubo/ModelRP2.git>).

Funding: This work was supported partly by the Brain Mapping by Integrated Neurotechnologies for Disease Studies (Brain/MINDS; JP20dm0207084 to YK, and JP20dm0207001 to SI) from the Japanese Agency for Medical Research and Development (AMED), CREST (JPMJCR20E4 to HU, JPMJCR1652 to HK and SI) from the Japan

Abstract

In behavioral learning, reward-related events are encoded into phasic dopamine (DA) signals in the brain. In particular, unexpected reward omission leads to a phasic decrease in DA (DA dip) in the striatum, which triggers long-term potentiation (LTP) in DA D2 receptor (D2R)-expressing spiny-projection neurons (D2 SPNs). While this LTP is required for reward discrimination, it is unclear how such a short DA-dip signal (0.5–2 s) is transferred through intracellular signaling to the coincidence detector, adenylyl cyclase (AC). In the present study, we built a computational model of D2 signaling to determine conditions for the DA-dip detection. The DA dip can be detected only if the basal DA signal sufficiently inhibits AC, and the DA-dip signal sufficiently disinhibits AC. We found that those two requirements were simultaneously satisfied only if two key molecules, D2R and regulators of G protein signaling (RGS) were balanced within a certain range; this balance has indeed been observed in experimental studies. We also found that high level of RGS was required for the detection of a 0.5-s short DA dip, and the analytical solutions for these requirements confirmed their universality. The imbalance between D2R and RGS is associated with schizophrenia and DYT1 dystonia, both of which are accompanied by abnormal striatal LTP. Our simulations suggest that D2 SPNs in patients with schizophrenia and DYT1 dystonia cannot detect short DA dips. We finally discussed that such psychiatric and movement disorders can be understood in terms of the imbalance between D2R and RGS.

Author summary

In our brain, learning and memory are strongly modulated by dopamine (DA) signals. Even a short absence of DA (0.5–2 s), called “DA dip,” triggers long-term memory formation, the underlying processes of which are hitherto largely unknown. Here, we examined

Science and Technology Agency (JST), the International Research Center for Neurointelligence (WPI-IRCN) at The University of Tokyo Institutes for Advanced Study (SY, HK, and SI), and JSPS KAKENHI (17K00404 and 20K12062 to HU, 17H06310 to SI, 26221001 to HK, and 19H03336 and 17H06311 to YK). The funders had no role in study design, data collection and analysis, decision to publish, or preparation of the manuscript.

Competing interests: The authors have declared that no competing interests exist.

how the DA dips are processed through a biochemical signaling network to generate long-term memory. Computer simulation and theoretical analyses showed that the DA-dip signal is processed only if the levels of two key molecules, DA D2 receptor (D2R) and regulators of G protein signaling (RGS), are both delicately balanced. This balance seems to be achieved in the healthy brain, whereas imbalance between D2R and RGS levels appear in patients with schizophrenia and DYT1 dystonia, both of which may manifest abnormal long-term memory. The D2R–RGS imbalances hamper DA-dip detectability, and thus disturb long-term memory formation, which may result in the symptoms of schizophrenia and dystonia. The balance between D2R and RGS appear to be finely regulated in the healthy brain to underpin normal learning and memory.

Introduction

In animals' reward learning, phasic dopamine (DA) signal in the brain conveys important information, called reward prediction errors [1,2]. Unexpected reward causes a phasic increase in striatal DA level for 0.2–1 s (DA burst), whereas unexpected reward omission leads to a transient decrease in DA for 0.5–2 s (DA dip) [3,4]. Such phasic DA signals are decoded into striatal synaptic plasticity that refines animal behavior to obtain larger rewards [1,5–8]. In particular, we previously found that 0.5–2-s DA dips triggered long-term potentiation (LTP) in dopamine D2 receptor (D2R)-expressing spiny-projection neurons (D2 SPNs) of the striatum [1,9]. The LTP is induced only if the DA dip coincides with the presynaptic release of glutamate and postsynaptic burst firing of a D2 SPN (pre–post pairing), under the presence of adenosine [1,10]. The DA dip needs to occur together with pre–post pairing, and this LTP is required for reward-discrimination learning [1]. Intracellularly, the DA-dip signal leads to the deactivation of D2R and then the decrease in the GTP-bound form of inhibitory G protein (G_i -GTP). The 0.5-s DA dip is similar to the timescale of the G-protein signaling (0.1–1 s) [11], raising a question about how the DA-dip signal is so reliably encoded into these signaling molecules. The same issue might be extended to psychiatric/movement disorders, because the alteration in D2R signaling and LTP in the striatum have been implicated [2,12,13].

We thus previously demonstrated using computational modeling, how such a rapid signal is encoded in the D2R signaling [10]. In the D2 LTP model, DA-bound D2R produces G_i -GTP, and the G_i -GTP inhibits adenylyl cyclase (AC), in particular, AC type 1 (AC1) as in our case [1,5]. In contrast, neuronal firing and adenosine signals elevate the levels of Ca^{2+} and the GTP form of stimulatory G protein (G_{olf} -GTP), respectively, both of which jointly activate AC1 [14,15]. Together, G_i , G_{olf} and Ca^{2+} signals are integrated at AC1 that functions as a coincidence detector [10,15]. For this to occur, the DA-dip signal itself must be transmitted to the AC. The AC activity triggers the longer molecular dynamics, such as increase in cyclic adenosine monophosphate (cAMP), resulting in the occurrence of LTP [1,5].

The similar DA-dip detection seems to be realized in the other subtype of AC, AC type 5 (AC5), because AC5 is abundantly expressed in the striatum [16,17]. G_{olf} -GTP alone sufficiently triggers the activity of AC5, while the AC5 activity is inhibited by G_i [18–20], and the DA-dip detection on AC5 should affect striatal synaptic plasticity [21] as well as the change of somatic neuronal excitability [22,23]. In particular, AC5 likely functions in the soma because somatic AC activity does not require the increase in Ca^{2+} level [5,19]. D2 signaling models have demonstrated that AC5 in D2 SPNs could detect short DA dips in conjunction with accompanying G_{olf} signals, referred to as the “tone sensing” mode [19,20,24]. In summary, in

either case of the type 1 or 5, DA-dip signal must be transmitted to AC if it is processed through G_i signaling for the coincidence detection.

The models of D2 signaling have demonstrated DA-dip detection by AC; however, these models consist of complicated signaling involving many parameters [10,19,24]. It is thus difficult to capture what components of the model parameters, i.e., molecular concentrations and kinetics constants, are essential for the transmission of DA-dip signal. Regarding our D2 LTP model [10], some of the parameters were well constrained by experimental measurements (e.g. Ca^{2+} signal [25]), while others were determined only based on order estimations or ratio constraints, and the DA-dip detection may also depend on remaining unconstrained factors. One way to examine the parameter dependence is a sensitivity analysis [26], i.e., exhaustive quantification of the changes in model output associated with changes in parameter values. However, this analysis is essentially phenomenological, which cannot address underlying principles. If the concentration dependence of the D2 model is analytically solved, it would provide precise parameter dependence as well as the underlying mechanisms simultaneously.

Further, molecular concentrations in D2 SPNs are altered depending on the age and health condition. In particular, the expression levels of D2R and its counteracting molecule, regulators of G protein signaling type 9–2 (RGS9–2), are both increased with age [27,28]. In schizophrenia, a psychiatric disorder, D2R shows supersensitivity [29,30], whereas the expression level of RGS9–2 is decreased [31,32]. In DYT1 dystonia, a movement disorder, the balance between D2R and RGS9–2 is conversely biased toward RGS9–2 [28]. Those psychiatric/movement disorders are also known to show abnormal LTP in D2 SPNs [1,2,33]. Thus, the D2 LTP model should be examined under the various concentrations of D2R and RGS9–2. However, it is still poorly understood how the concentrations of D2R and RGS9–2 are related to LTP and brain function/dysfunction.

In the present study, we selectively targeted the D2R– G_i –AC part (D2 model) from the previous D2-LTP model to clarify the requirements for the DA-dip detection. We first examined the concentration dependence of five representative molecules (S1 Table), and revealed that D2R and RGS must be balanced within a narrow concentration range, which was consistent with their age-dependent co-increase observed in an experiment [28]. The balance requirement appeared to be valid under both non-competitive and competitive G_i inhibition of AC, and theoretical analyses further proved the universality of the balance requirements. If the balance was biased toward D2R as in schizophrenia [29–32], the increased D2R activity produced excess amount of G_i -GTP, disrupting the DA-dip detection for LTP. If the balance was biased toward RGS as in the case of DYT1 dystonia [28], the smaller amount of G_i -GTP also disturbed the DA-dip detection. We further discuss the relationship among the D2R–RGS balance, LTP, and disease mechanisms.

Methods

Overview of modeling

We selected the D2R– G_i –AC part from the previous kinetic model of LTP in striatal D2 SPNs (Fig 1A, gray shaded area) [10], and examined the “D2 model” to address whether DA-dip signal was transmitted to AC with a time resolution of 0.5–2 s [3,4]. In our primary target experiment [1], D2 SPNs accepted three types of input stimulation: and a continuous pharmacological activation of adenosine A2A receptors (A2AR; Fig 1B), tonic DA signal and its pause (DA dip; Fig 1C), and phasic pre–post pairing (Fig 1D). According to the knowledge of intracellular signaling [9], the tonic signal of DA activates D2R, leading to the GDP/GTP exchange in G_i . The produced G_i -GTP inhibits the activity of AC1, in particular, in the presence of $G_{\beta\gamma}$ (S1 Table) [18]. The G_i -GTP is rapidly hydrolyzed due to GTPase activating

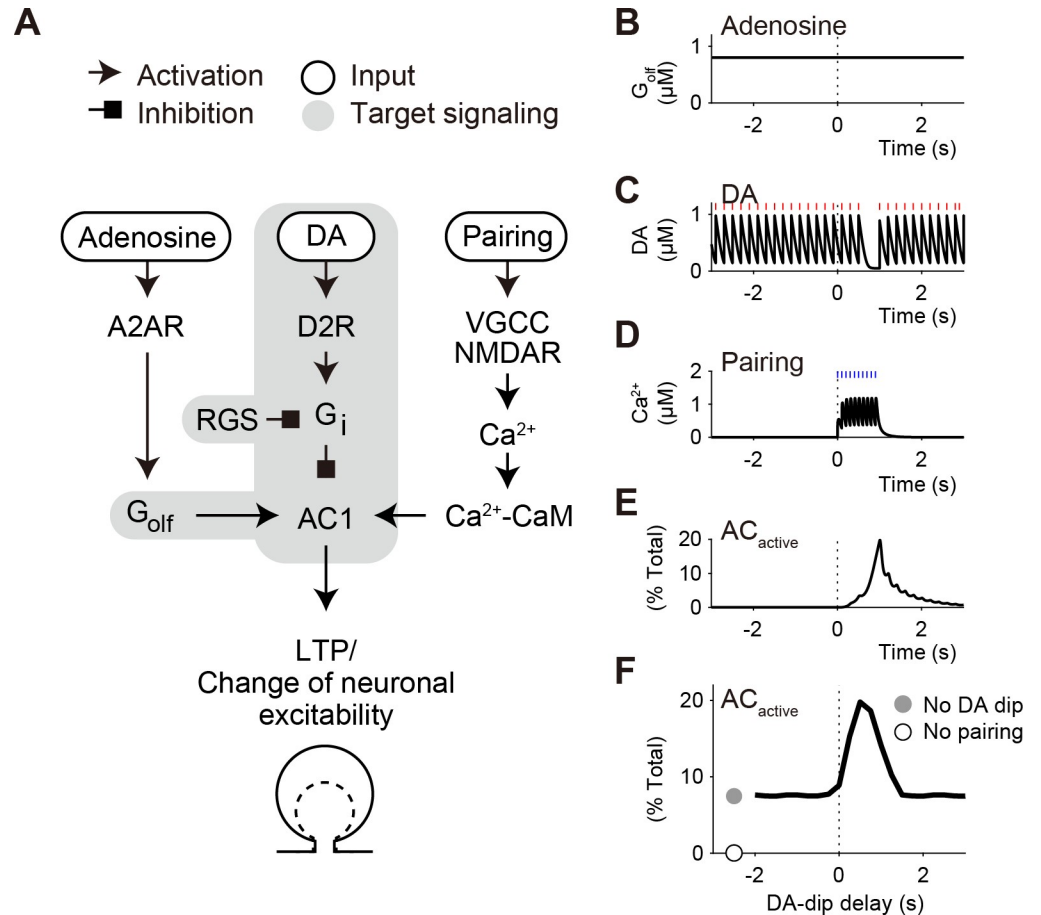


Fig 1. The D2 model performs the coincidence detection between DA dip and pre-post pairing. (A) Three signaling cascades toward AC1 for LTP in D2 SPNs of the striatum [10]. First, adenosine stimulates A2AR, which produces G_{olf}-GTP to activate AC1. Second, basal DA signal leads to the activity of D2R, and then produces a GTP from G_i (G_i-GTP), which inhibits the AC1 activity. Third, pre-post pairing signal leads to the postsynaptic increase in Ca²⁺-CaM that stimulates AC1. Signaling in the gray shaded area is modeled in the present D2 model. (B-F) Coincidence detection between DA dip and pre-post pairing. (B) In Iino et al. (2020), A2AR were pharmacologically activated to give a continuous signal of G_{olf}-GTP [1]. (C) DA fibers are optogenetically stimulated tonically at 5Hz (red lines). The tonic stimulation accompanies a 0.5-s pause (DA dip, t_{DA,delay} = 0.5 s), as a representation of unexpected reward omission. (D) Sensory/action signals are represented by pre-post pairing at 10 times and 10 Hz (blue lines), which gives a transient Ca²⁺ signal. (E) The G_{olf}, G_i, and Ca²⁺-CaM signals transiently activates AC1 (AC_{active}). (F) A timing window for DA-dip delay on the maximal amplitudes of AC_{active}. The D2 model is simulated under the non-competitive binding among G_{olf}, G_i, and Ca²⁺-CaM (standard non-competitive model; see S1 Fig and section A in S1 Appendix).

<https://doi.org/10.1371/journal.pcbi.1009364.g001>

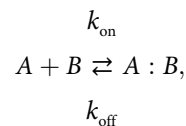
proteins, especially, RGS9-2 in the striatum [27,34,35]. Thus, a pause of tonic DA increases the GDP-bound form of G_i (G_i-GDP), which results in the detachment of G_i-GDP from AC1, and the G_i-free AC1 is disinhibited. In contrast, pre-post pairing generates a transient signal of Ca²⁺/calmodulin (Ca²⁺-CaM) (Fig 1D), and A2AR activity produces a continuous signal of G_{olf}-GTP (Fig 1B). The Ca²⁺-CaM and G_{olf}-GTP both bind and activate AC1 in a synergistic manner (Fig 1E) [14,15]. The AC1 activity produces cAMP, which activates cAMP-dependent protein kinase (PKA), and enhances the induction of LTP or other neuronal functions. The DA-dip also disinhibits another subtype of AC, AC5 [20,24]. The disinhibited AC5 is activated by the binding of G_{olf}-GTP alone [18,36], and Ca²⁺-CaM is not required for the activation (S1B and S2B Figs) [37]. We chose the shared part of both AC1 and AC5 as the D2 model to examine the DA-dip detectability in AC (see the subsection “Readouts”).

In the following subsection, we described the basic principles of kinetic formulation, input signals, and readouts of the D2 model. The detailed description of the D2 model is provided in **section A in S1 Appendix** and **S1 and S2 Figs**, and molecular concentrations and kinetic constants are summarized in **S1 and S2 Tables**, respectively. Compared to the previous D2 LTP model, some parameters were updated according to experimental evidence. We thus confirmed that the updated set of parameters provided a time window as shown in the previous D2 LTP model (**Fig 1F**) [10], and it was used as a standard set of parameters. Computer simulation of the D2 model was carried out using MATLAB SimBiology (R2020a; MathWorks). The developed MATLAB code and its SBML-style files are available at the public repository GitHub (<https://github.com/urakubo/ModelRP2.git>).

Binding and enzymatic reactions

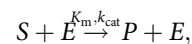
All molecular interactions in the D2 model were represented by binding and enzymatic reactions under the mass assumption [10,38,39]. In the formulation, “:” denotes non-covalent binding between molecules. $G_{\beta};G_{\gamma}$ is exceptionally denoted by $G_{\beta\gamma}$, because $G_{\beta};G_{\gamma}$ is known to form a tight complex [40]. GTP and GDP forms of G_X are represented by G_X -GTP and G_X -GDP, respectively, and Ca^{2+} /calmodulin is represented by Ca^{2+} -CaM. $[X]$ denotes time-varying molecular concentration, $[X]_{tot}$ denotes the total concentration, and $[X]_{buff}$ denotes the buffered concentration. $[X]_{basal}$ denotes molecular concentration at the basal state ($d[X]/dt = 0$ under $[DA] = [DA]_{basal}$), $[X]_{dip}$ denotes molecular concentration at the DA-dip state ($d[X]/dt = 0$ under $[DA] = [DA]_{dip}$). $[DA]_{basal}$ and $[DA]_{dip}$ are described in the subsection “Inputs.”

A binding reaction in which A binds to B to form $A:B$ was expressed by the following equation:



$$\frac{d[A : B]}{dt} = k_{on}[A][B] - k_{off}[AB], \quad (1)$$

where k_{on} and k_{off} are the rate constants for the forward and backward reactions, respectively. Here, k_{off}/k_{on} is known as the dissociation constant, K_d . Enzymatic reactions were modeled based on the Michaelis-Menten (MM) equation:



$$\frac{d[P]}{dt} = \frac{k_{cat}[E][S]}{K_m + [S]}, \quad (2)$$

where S , E , and P denote substrate, enzyme, and product, respectively, and K_m and k_{cat} are the Michaelis constant and product turnover rate, respectively. We did not consider E - S complexes for simplicity, similarly to a previous study [41].

Inputs

In Iino et al. (2020), channelrhodopsin-2-expressed DA fibers were stimulated with 5-Hz light stimulation with a 0.4-s pause, and the pause signal was successfully observed as a DA-dip signal of extracellular DA dynamics [1]. However, the penetration of an observation probe (5~8 μ m diameter) might interfere with the DA dynamics, because the cycle of DA release,

diffusion, and uptake is known to occur only in a span of ~10 μm [42]. Recent DA observation using an ultrafast fluorescent probe shows the faster dynamics of DA ($t_{1/2} \sim 0.1$ s) [43,44]. Thus, based on a preceding model [45], we first simulated the rapid concentration dynamics of DA, [DA], as follows (Figs 1C and 2A):

$$\{t_{DA}^i\}_{i=-\infty}^{\infty} = \{\dots, -0.4 \text{ s}, -0.2 \text{ s}, 0 \text{ s}, T_{dip}, T_{dip} + 0.2 \text{ s}, T_{dip} + 0.4 \text{ s}, \dots\},$$

$$\frac{d}{dt}[DA] = [DA]_{opto} \sum_i \delta(t - t_{DA}^i - t_{DA, delay}) - \frac{k_{cat, DAT} K_{m, DAT} [DAT] ([DA] - [DA]_{dip})}{(K_{m, DAT} + [DA])(K_{m, DAT} + [DA]_{dip})}, \quad (3)$$

where T_{dip} is the duration of a DA pause, $t_{DA, delay}$ is the onset time of the DA pause, $[DA]_{dip}$ is the bottom concentration of produced DA dip, and $[DA]_{opto}$ is the amplitude of DA signal by a single light pulse. $k_{cat, DAT}[DAT]$ and $[DA]_{opto}$ were determined so as to give an average concentration of 0.5 μM and a half-valued period of 0.1 s [1,44].

We next characterized the DA-dip signal as a square wave dip of [DA] (Fig 2B):

$$[DA] = \begin{cases} [DA]_{basal} & (t < 0, T_{dip} \leq t) \\ [DA]_{dip} & (0 \leq t < T_{dip}) \end{cases}, \quad (4)$$

Here, we set $[DA]_{basal} = 0.5 \mu\text{M}$ and $[DA]_{dip} = 0.05 \mu\text{M}$ unless otherwise stated (Fig 2B). Those levels of DA have been estimated based on a reference experiment (S1 Table) [1]. We finally gave a stepwise-decreasing signal of DA to quantify the DA-dip detection in the response of AC:

$$[DA] = \begin{cases} [DA]_{basal} & (t < 0) \\ [DA]_{dip} & (t \geq 0) \end{cases}. \quad (5)$$

In Iino et al. (2020), A2AR was continuously activated to produce G_{olf} -GTP with a constant rate [1]. The G_{olf} -GTP is known to bind to a specific site of AC, while it is autonomously hydrolyzed and detached from the AC [46]. The dynamics of G_{olf} -GTP was simply modeled as a constant concentration of buffered G_{olf} [G_{olf}]_{buff} (Fig 1B).

We also simulated a pre-post pairing-induced dynamics of Ca^{2+} . The pre-post pairing was constituted of 10-consecutive elemental pairs at 10 Hz (Fig 1D):

$$\{t_{pre-post}^i\}_{i=1}^{10} = \{0 \text{ s}, 0.1 \text{ s}, 0.2 \text{ s}, \dots, 0.9 \text{ s}\}. \quad (6)$$

Each pairing led to Ca^{2+} influx via voltage-gated Ca^{2+} channels (VGCC) and *N*-Methyl-*D*-aspartate receptors (NMDAR). The Ca^{2+} bound to CaM, while free Ca^{2+} was uptaken by a Ca^{2+} pump. The Ca^{2+} -CaM further bound to a specific site of AC. Detailed scheme and parameters of the Ca^{2+} signal are described in Urakubo et al. (2020) [10], and the MATLAB code of the full D2 model is available at the public repository GitHub (<https://github.com/urakubo/ModelRP2.git>).

Readouts

G_{olf} and Ca^{2+} -CaM synergistically activate AC1 [14,15], and G_{olf} alone sufficiently activate AC5 [37]. The G_{olf} -dependent activity of AC5 is inhibited by G_i , and the Ca^{2+} -CaM-dependent component of AC1 activity is also inhibited by G_i , while the G_{olf} -dependent component of AC1 activity is only weakly inhibited by G_i [18]. We here assumed that the G_{olf} - and Ca^{2+} -CaM-dependent synergistic activity of AC1 was strongly inhibited by G_i . G_{olf} , G_i , and Ca^{2+} -CaM are known to have their specific binding sites at AC1/5 [36,47,48], and molecular

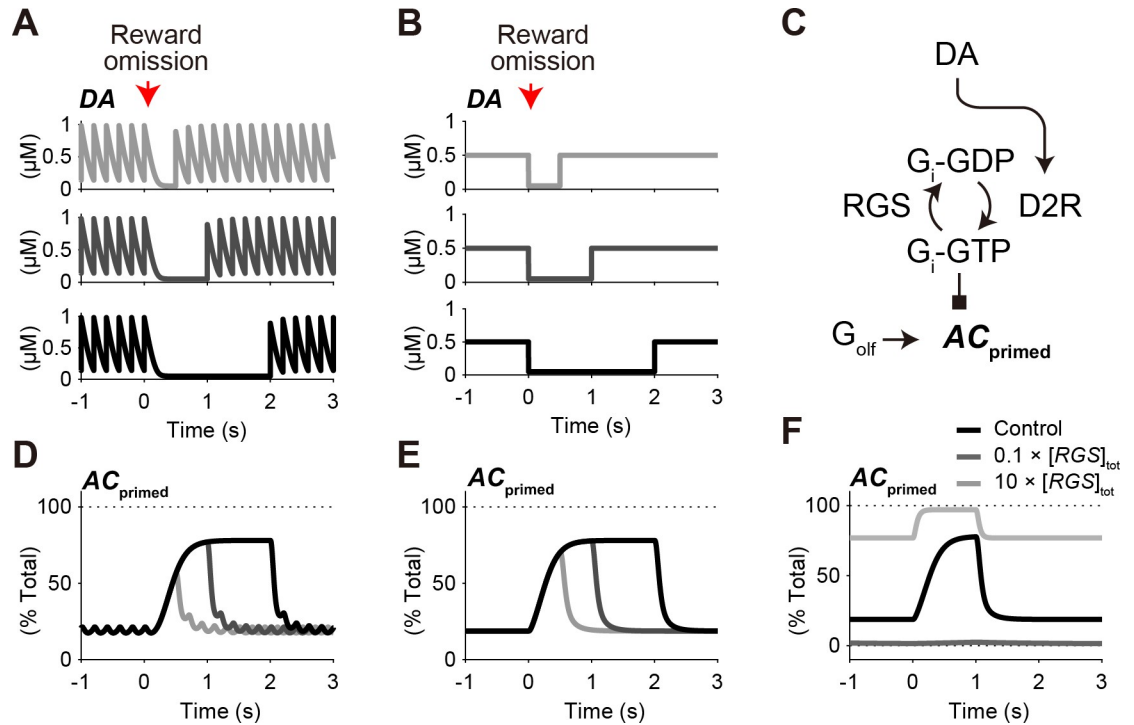


Fig 2. Characterization of optogenetically-evoked DA dynamics as a square wave dip. (A) Simulation of optogenetically-evoked DA dynamics (5 Hz) and their pauses for 0.5 s, 1.0 s, and 2.0 s (top, middle, and bottom, respectively). The tonic optogenetic stimulation is set to generate 0.5 μM DA on average, and the DA pause is set to give 0.05 μM DA at bottom levels (see Methods). (B) Characterization of the optogenetic DA signals as square wave dips. (C) Introduction of $\text{AC}_{\text{primed}}$ as the G_i -free and G_{olf} -bound state of AC. Further Ca^{2+} stimulation leads to the activity of AC1. In the case of AC5, $\text{AC}_{\text{primed}}$ corresponds to a normalized activity of AC. (D) Dynamics of $\text{AC}_{\text{primed}}$ in response to the optogenetically-evoked DA signals. (E) Dynamics of $\text{AC}_{\text{primed}}$ in response to the square-wave DA dips. (F) Appropriate range of $[\text{RGS}]_{\text{tot}}$ is required for the response of $\text{AC}_{\text{primed}}$. Square-wave DA dips are given with a duration of 1 s. $\text{AC}_{\text{primed}}$ reaches almost the maximal level even with the basal DA signal if $[\text{RGS}]_{\text{tot}}$ is set to be 10 times higher than the standard concentration (9 μM , light gray line), and $\text{AC}_{\text{primed}}$ does not show any increase if $[\text{RGS}]_{\text{tot}}$ is 10 times lower than the standard concentration (0.09 μM , dark gray line).

<https://doi.org/10.1371/journal.pcbi.1009364.g002>

dynamics simulation shows that AC5 forms an inactive ternary complex with G_{olf} and G_i [20]. Those pieces of evidence support the idea that G_i non-competitively inhibits AC, i.e., G_{olf} , G_i , and Ca^{2+} -CaM independently bind to AC, and the G_i -binding itself inhibits the enzymatic activity of AC (non-competitive inhibition; S1 Fig). In contrast, biochemical studies suggest that G_i competitively inhibits AC5 [36,49], i.e., G_i inhibits the AC activity by prohibiting the binding of activators, i.e., G_{olf} and Ca^{2+} -CaM (S2 Fig). In short, the mechanism of G_i inhibition is currently obscure even in the case of well-studied AC5. Considering this situation, we examined two extreme cases of the G_i inhibition: 100% non-competitive binding among G_i , G_{olf} , and Ca^{2+} -CaM, (standard non-competitive model) and 100% competitive binding between G_i and the other two molecules (competitive model), and $\text{AC}_{\text{primed}}$ was introduced as a shared readout of AC1 and AC5.

Standard non-competitive model. The concentration of active-state AC, $[\text{AC}_{\text{active}}]$, was defined by the following equation (S1 Fig):

$$\frac{[\text{AC}_{\text{active}}]}{[\text{AC}]_{\text{tot}}} = \begin{cases} \frac{[\text{AC}_{\text{i}}^{\text{site}}]}{[\text{AC}]_{\text{tot}}} \cdot \frac{[\text{AC}_{\text{olf}}^{\text{site}} : \text{G}_{\text{olf}}]}{[\text{AC}]_{\text{tot}}} \cdot \sum_i \frac{[\text{AC}_{\text{CaM}}^{\text{site}} : \text{Ca}^{2+} - \text{CaM}_i]}{[\text{AC}]_{\text{tot}}} & (\text{AC1}) \\ \frac{[\text{AC}_{\text{i}}^{\text{site}}]}{[\text{AC}]_{\text{tot}}} \cdot \frac{[\text{AC}_{\text{olf}}^{\text{site}} : \text{G}_{\text{olf}}]}{[\text{AC}]_{\text{tot}}} & (\text{AC5}) \end{cases}, \quad (7)$$

where AC_i^{site} , AC_{olf}^{site} , and AC_{CaM}^{site} denote the binding sites of AC for G_i , G_{olf} , and Ca^{2+} -CaM, respectively, and $i = 1, \dots, 9$ denote the states of Ca^{2+} -CaM. Here, $[AC_i^{site}]$ denotes the concentration of G_i -free AC, i.e., $[AC_i^{site}] = [AC]_{tot} - [AC_i^{site} : G_i]$. We then selected the shared part of AC1 and AC5, as a primed state of AC for the activity:

$$AC_{primed} = \frac{[AC_i^{site}]}{[AC]_{tot}} \cdot \frac{[AC_{olf}^{site} : G_{olf}]}{[AC]_{tot}} \cdot \frac{K_{d,Golf} + [G_{olf}]_{buff}}{[G_{olf}]_{buff}} \tag{8}$$

where $[G_{olf}]_{buff}/\{K_{d,Golf} + [G_{olf}]_{buff}\}$ denotes the binding ratio of AC to G_{olf} . If $[G_{olf}]_{buff}$ is a constant,

$$\frac{[AC_{olf}^{site} : G_{olf}]}{[AC]_{tot}} = \frac{[G_{olf}]_{buff}}{K_{d,Golf} + [G_{olf}]_{buff}} \tag{9}$$

Thus, AC_{primed} is simply $[AC_i^{site}]/[AC]_{tot}$ under the constant $[G_{olf}]_{buff}$. All simulation and analyses were conducted on the standard non-competitive model unless otherwise stated.

Competitive model. We defined the concentration of active-state AC, $[AC_{active}]$, under the situation of 100%-competitive binding between G_i and the other two molecules, G_{olf} and Ca^{2+} -CaM (S2 Fig):

$$\frac{[AC_{active}]}{[AC]_{tot}} = \begin{cases} \sum_i \frac{[G_{olf} : AC : Ca^{2+}-CaM_i]}{[AC]_{tot}} & \text{(AC1)} \\ \frac{[G_{olf} : AC]}{[AC]_{tot}} & \text{(AC5)} \end{cases}, \tag{10}$$

where $[G_{olf} : AC : Ca^{2+}-CaM_i]$ denotes the concentration of AC that binds to both G_{olf} and Ca^{2+} -CaM, but not to G_i . The G_{olf} binding and G_i unbinding are shared requirements for the activities of AC1 and AC5 (S2 Fig). We thus picked up the shared part of AC1 and AC5, as a primed state of AC for the activity, AC_{primed} , as:

$$AC_{primed} = \frac{[G_{olf} : AC]}{[AC]_{tot}} \cdot \frac{K_{d,Golf} + [G_{olf}]_{buff}}{[G_{olf}]_{buff}} \tag{11}$$

In both non-competitive and competitive models, AC_{primed} was set to be a readout. AC_{primed} is a dimensionless value ($0 \leq AC_{primed} \leq 1$), and $0\% \leq AC_{primed} \leq 100\%$ was used in the description. We also introduced AC_{basal} and AC_{dip} to represent two steady states of AC_{primed} , i.e., $AC_{basal} = \lim_{t \rightarrow \infty} AC_{primed}(t)$ where $[DA] = [DA]_{basal}$, and $AC_{dip} = \lim_{t \rightarrow \infty} AC_{primed}(t)$ where $[DA] = [DA]_{dip}$.

DA-dip duration dependence in AC_{primed}

Here, we quantified the DA-dip duration-dependent response of AC_{primed} using the following equation:

$$\langle AC_{primed} \rangle_{T_{dip}} = \frac{1}{T_{dip}} \int_0^{T_{dip}} AC_{primed}(t) dt. \tag{12}$$

$\langle AC_{primed} \rangle_{T_{dip}}$ represents the average increase in AC_{primed} during the DA-dip period $[0, T_{dip}]$ in Eq (4).

Concentrations of D2R and RGS under healthy and pathologic conditions

Four pairs of $[D2R]_{tot}$ and $[RGS]_{tot}$ were set to represent a healthy adult, healthy infant, and patients with DYT1 dystonia and schizophrenia. $[D2R]_{tot}$ and $[RGS]_{tot}$ in the standard set of parameters were used for the healthy-adult model, and $0.5 \times [D2R]_{tot}$ and $0.5 \times [RGS]_{tot}$ were set for the healthy-infant model, because Bonsi et al. have observed a ~ 0.4 -fold simultaneous decrease in their expression levels in the striatum of infant mice (postnatal day 7) [28]. Such a decrease has been seen in other studies as well [50,51]. A parameter set of $4.0 \times [D2R]_{tot}$ and $0.5 \times [RGS]_{tot}$ was used for the schizophrenia model, because D2 blockers need to occupy 70–85% of the total D2R to give clinical effects while avoiding side effects [52,53], and the level of RGS seems to decrease by 10–75% in schizophrenia [31,32]. A parameter set of $0.5 \times [D2R]_{tot}$ and $2.0 \times [RGS]_{tot}$ was used for the dystonia model, because Bonsi et al. have observed a 0.7-fold D2R decrease and 1.6-fold RGS increase in the protein expression levels of the striatal detergent-resistant membranes (DRM) in a mouse model of DYT1 dystonia [28], and another study has shown a ~ 0.25 -fold decrease in the activity of striatal D2R in another mouse model of DYT1 dystonia [54]. Note that those values were determined only for exemplifying purpose, and the actual concentrations depend on the subjects.

Results

Characterization of DA pause as a square wave dip

The updated D2 model was first simulated to confirm the occurrence of a time window for DA-dip delay on the activity of AC1 (Fig 1) [10]. In this simulation, we applied the D2 model to three types of inputs (Fig 1A): a constant signal of G_{olf} (Fig 1B), optogenetically-evoked tonic DA signal with a 0.5-s pause (Fig 1C), and 1-s pre–post pairing (Fig 1D). Those inputs resulted in a transient activity of AC1, AC_{active} (Fig 1E), and the AC1 activity depended on the delay of DA pause, $t_{DA, delay}$ (Fig 1F), as shown in the previous D2 LTP model [10]. The activity of AC1 is known to produce cAMP, leading to neuronal functions such as synaptic plasticity (Fig 1A).

Among the three input signals, DA pause is particularly interesting. The rapid dynamics of DA resulted in a fluctuating DA signal even under the basal state, and the 0.5-s DA pause appeared to be a minor event (Fig 1C). We thus examined how the DA-pause signal was transmitted to AC, by characterizing it as a square wave dip of DA (Fig 2A and 2B), and the normalized level of G_i -free and G_{olf} -bound AC, AC_{primed} , was observed as a readout (see Methods; Fig 2C). In the dynamics of AC_{primed} , the optogenetically-evoked signals of DA were well characterized by the square wave dips of DA (Fig 2D and 2E), because the fluctuation in the basal DA signal was attenuated through the D2R– G_i –AC signaling pathway (S3 Fig).

The response of AC_{primed} was dependent not only on the DA dynamics, but also on the concentrations of other constituent molecules (Fig 2F). If the concentration of RGS, $[RGS]_{tot}$, was set to be 10 times higher than the standard concentration (S1 Table), AC_{primed} showed $\sim 80\%$ of the maximal activity even with the basal DA signal (Fig 2F, light gray line). In this case, there was only small room for further activation. By contrast, if $[RGS]_{tot}$ was set to be 10 times lower than the standard concentration, AC_{primed} did not show any activity even during the DA dip (Fig 2F, dark gray line). We thus raised a next question: what are requirements on the parameters, i.e., molecular concentration and kinetic constants, for the DA-dip detection?

Amplitudes of AC_{primed} for DA-dip detection

Then, using a stepwise decreasing signal of DA (Eq (4)), we examined the molecular concentrations required for DA-dip detection (Fig 3A, top). Here, the DA-dip detectability was

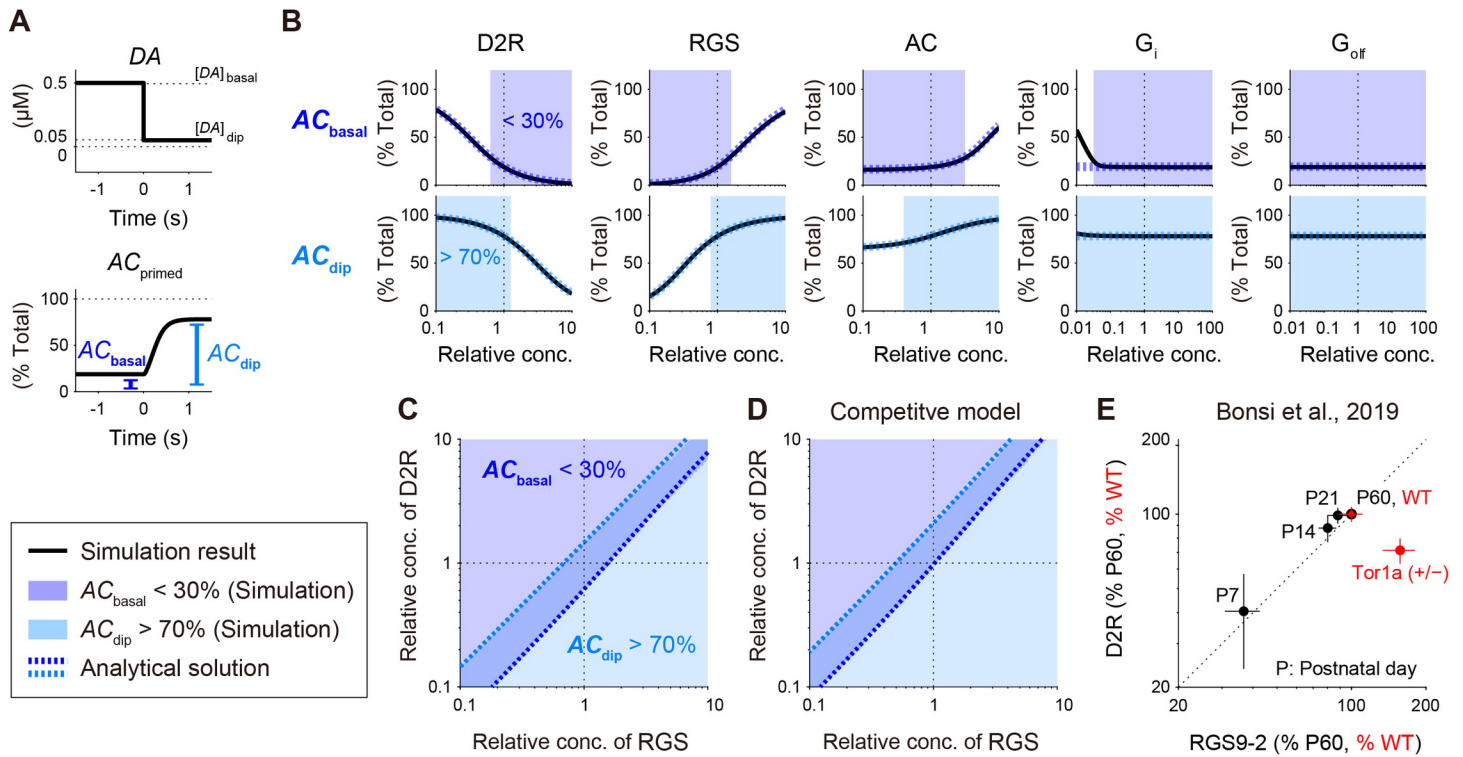


Fig 3. DA-dip detectable region appears between two increasing boundaries in the space of D2R and RGS. (A) Introduction of two measures, AC_{basal} and AC_{dip} , to quantify DA-dip detectability. AC_{primed} under the basal DA signal, AC_{basal} , should be low, whereas that during a DA dip, AC_{dip} , should be high. (B) Concentration requirements for the DA-dip detection under the two measures. While D2R, RGS, AC, G_i, and G_{olf} are targeted, AC_{basal} and AC_{dip} are measured under the altered concentrations of one of the target molecules. Simulation results (black solid lines) and analytical solutions (blue and light blue dotted lines, Eq (23)) are plotted. $AC_{\text{basal}} < 30\%$ and $AC_{\text{dip}} > 70\%$ are highlighted as the regions necessary for DA-dip detection. (C) $AC_{\text{basal}} < 30\%$ and $AC_{\text{dip}} > 70\%$ in the space of $[D2R]_{\text{tot}}$ and $[RGS]_{\text{tot}}$. Analytical isolines of $AC_{\text{basal}} = 30\%$ and $AC_{\text{dip}} = 70\%$ are overlaid. (D) Same as panel C, but the D2 model is based on the competitive binding between G_{olf} and G_i (See S2 Fig). (E) Age-dependent expression levels of RGS9–2 and D2R proteins (black points) and their altered levels in a mouse model of DYT1 dystonia (*Tor1a* (+/-), red points) in Bonsi et al. [28]. Data are taken from the DRM fraction of the mouse striatum (Figs 1A and 2C of Bonsi et al. [28]; modified under Creative Commons Attribution 3.0). P7, . . . , P60 denote mouse postnatal days. Data are normalized by the expression levels in P60 or wild type (WT).

<https://doi.org/10.1371/journal.pcbi.1009364.g003>

quantified by two variables: AC_{basal} and AC_{dip} (Fig 3A). AC_{basal} denotes the steady-state level of AC_{primed} under $[DA] = [DA]_{\text{basal}}$ (Fig 3A, dark blue; see Methods), and AC_{dip} denotes the steady-state level of AC_{primed} under $[DA] = [DA]_{\text{dip}}$ (Fig 3A, light blue). We observed AC_{basal} and AC_{dip} if the concentration of one of the five constituent molecules, $[D2R]_{\text{tot}}$, $[RGS]_{\text{tot}}$, $[AC]_{\text{tot}}$, $[G_i]_{\text{tot}}$, and $[G_{\text{olf}}]_{\text{buff}}$ was varied ranging from 0.1-fold to 10-fold, while the concentrations of other molecules were kept unchanged (Fig 3B and S1 Table). First, we observed that neither AC_{basal} nor AC_{dip} was sensitive to $[G_i]_{\text{tot}}$ and $[G_{\text{olf}}]_{\text{buff}}$ if they were higher than 4% of the standard concentration (Fig 3B, second right and right, black lines), while AC_{basal} and AC_{dip} were both highly sensitive to $[D2R]_{\text{tot}}$ and $[RGS]_{\text{tot}}$ (Fig 3B, left and second left, black lines). This is because the concentrations of D2R and RGS determined the available amount of G_i-free AC for the activity. Here, for convenience, the regions that satisfies $AC_{\text{basal}} < 30\%$ and $AC_{\text{dip}} > 70\%$ were highlighted as the regions that enabled DA-dip detection (blue and light-blue shaded areas, respectively; Fig 3B). In the cases of $[D2R]_{\text{tot}}$, $[RGS]_{\text{tot}}$, and $[AC]_{\text{tot}}$, the regions that satisfied $AC_{\text{basal}} < 30\%$ (blue) and those that fulfilled $AC_{\text{dip}} > 70\%$ (light blue) occupied the opposite ends of the concentrations, and the intersection of the two regions satisfying both of them were limited within narrow concentration ranges. Note that the requirement of higher $[D2R]_{\text{tot}}$ for smaller AC_{basal} has been shown as the requirement of higher

$[DA]_{\text{basal}}$ in a previous study (Fig 3B, left, top) [19], and the requirement of lower $[D2R]_{\text{tot}}$ for higher AC_{dip} has also been shown as the requirement of lower $[DA]_{\text{dip}}$ in another study [24].

Because the windows for DA detection in $[D2R]_{\text{tot}}$ and $[RGS]_{\text{tot}}$ were particularly narrow, we further plotted their two-way relationship in a 2D space (Fig 3C). The DA-dip detectable region in $[D2R]_{\text{tot}}$ had a clear positive relationship with that in $[RGS]_{\text{tot}}$; the higher $[D2R]_{\text{tot}}$ requires the higher $[RGS]_{\text{tot}}$ for the detection of a DA dip (Fig 3C). Very interestingly, Bonsi et al. (2019) have shown that the expression level of striatal RGS9–2 has a similar positive relationship with that of D2R (Fig 3E, black points) in postnatal development of mice, during which both their expressions are increased [28]. They have further examined a DYT1 dystonia model (*Tor1a*^{+/-}-knock-out mice), and it shows a simultaneous decrease in the gross expression levels of D2R and RGS9–2. However, because DYT1 dystonia alters protein trafficking, the expression level of RGS9–2 is selectively increased in the fraction of DRM where D2Rs is located [28,55], and the perpendicular change appeared in the space of D2R and RGS9–2 (Fig 3D, red points). In the scheme of the D2 model, the disruption of the D2R–RGS balance makes DA dip undetectable, thus DYT1 dystonia cannot show DA-dip dependence in striatal LTP.

The requirement of the D2R–RGS balance appeared under $[DA]_{\text{basal}} = 0.5 \mu\text{M}$ and $[DA]_{\text{dip}} = 0.05 \mu\text{M}$. The concentrations of DA were determined based on experimental measurements (S1 Table) [1]; however, at least $[DA]_{\text{basal}}$ is known to depend on the specific situation [56,57]. We thus simulated multiple cases of $[DA]_{\text{basal}}$ and $[DA]_{\text{dip}}$, and found that they affected the regions of $AC_{\text{basal}} < 30\%$ and $AC_{\text{dip}} > 70\%$, and the region that satisfied both of them disappeared depending on the pair of $[DA]_{\text{basal}}$ and $[DA]_{\text{dip}}$ (S5 Fig). Nevertheless, the DA-dip detectable region in $[D2R]_{\text{tot}}$ always had a positive relationship with that in $[RGS]_{\text{tot}}$ (S5A and S5B Fig; left), and the D2R–RGS balance was always required regardless of the pair of $[DA]_{\text{basal}}$ and $[DA]_{\text{dip}}$, if we considered analytical solutions that explain these boundaries (S5 Fig, dotted lines; see the subsection “Analytical formulation”).

All the simulations so far were based on the D2 model under 100%-non-competitive binding between G_{olf} and G_i (standard non-competitive model; S1 Fig and section A in S1 Appendix). It is known that G_{olf} stimulates both AC1 and AC5, and G_i inhibits their activities [58]. However, even in well studied AC5, it is still under investigation whether AC is inhibited by G_i through non-competitive inhibition or the allosteric exclusion of G_{olf} binding [20,59]. We thus simulated the D2 model under 100%-competitive binding between G_{olf} and G_i (competitive model; S2 Fig and section A in S1 Appendix). The simulation results were similar to those in the standard non-competitive model (S4A and S4B Fig), and the requirements of the D2R–RGS balance also appeared only with a slight bias toward RGS (Fig 3D). The actual G_i inhibition should fall in between the 100%-competitive and non-competitive models. Thus, the requirements of the D2R–RGS balance was robust to the mechanisms of G_i inhibition.

In the simulation, the concentration of G_{olf} affected AC_{primed} only in the competitive model (Figs 3B and S4B, right). This is because the binding of G_{olf} to AC decreased the availability of G_{olf} -free AC for G_i inhibition, and the increase in $[G_{\text{olf}}]_{\text{buff}}$ led to a simultaneous increase in AC_{basal} and AC_{dip} , which decreased the dynamic range of AC_{primed} (S4B Fig, right). Conversely, if $[G_{\text{olf}}]_{\text{buff}}$ was set to be low, the dynamic range was restored (S4B Fig, right); however, the maximal activity of AC became small. As a result, there appeared to be an optimal $[G_{\text{olf}}]_{\text{buff}}$ for $\Delta AC_{\text{active}}$ where $\Delta AC_{\text{active}} = AC_{\text{active}}|_{[DA]=[DA]_{\text{dip}}} - AC_{\text{active}}|_{[DA]=[DA]_{\text{basal}}}$ (S4C Fig). It was consistent with the simulation results in a previous study [20].

Rapid response of AC_{primed} for DA-dip detection

The DA-dip detection depends not only on the steady-state levels of AC_{primed} , but also on its time constant. That is, the time constant of G_i unbinding must be shorter than the DA-dip

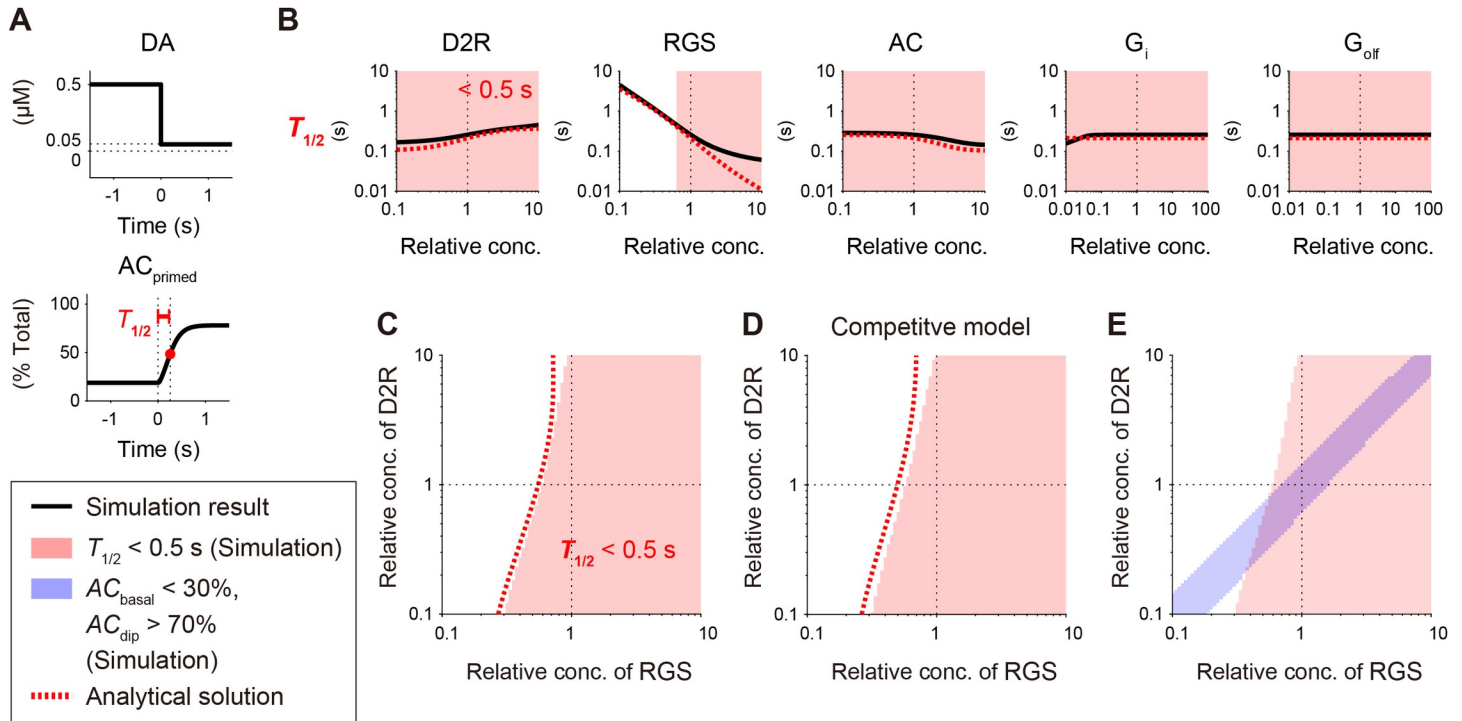


Fig 4. DA dip detection requires a certain concentration of RGS. (A) The third measure to quantify DA-dip detectability. Sudden decrease in the basal DA signal disinhibits AC with a half-maximal time, $T_{1/2}$, which needs to be small for detection of a short (~0.5 s) DA-dip. (B) Concentration dependence of $T_{1/2}$. Five molecules were targeted, and the simulation results (black solid lines) and analytical solutions (red dotted line, Eq (24)) were plotted. $T_{1/2} < 0.5$ s were highlighted in pink as the region that allows detection of the DA dip. (C) $T_{1/2} < 0.5$ s (pink) in the space of $[D2R]_{tot}$ and $[RGS]_{tot}$. (D) Same as panel C, but the DA model was based on the competitive binding between G_{olf} and G_i (See S1 and S2 Figs). (E) The area of $T_{1/2} < 0.5$ s (pink shaded area in (C)) was overlapped with the region that satisfies both $AC_{basal} < 30\%$ and $AC_{dip} > 70\%$ (blue shaded area). The ~0.5-s DA dips can only be detected in the overlapping area.

<https://doi.org/10.1371/journal.pcbi.1009364.g004>

duration, because otherwise the DA-dip signal would not appear in the change of AC_{primed} [19]. We thus evaluated it using a variable, $T_{1/2}$, where $T_{1/2} (> 0$ s) denotes the half maximal time of AC_{primed} after a sudden DA decrease (Fig 4A). Note that exponential fits were not utilized to quantify the increasing time constant because the AC_{primed} response did not always grow in an exponential manner. We obtained $T_{1/2}$ using the same set of molecular concentrations as in Fig 3B, and found that $T_{1/2}$ became less than 0.5 s only if $[RGS]_{tot}$ exceeded a certain level (Fig 4B, red shaded areas). Then, we plotted the DA-dip detectable area in the 2D space of $[D2R]_{tot}$ and $[RGS]_{tot}$ and found a slight dependence on $[D2R]_{tot}$ (Fig 4C). We finally overlaid this plot with the requirements on AC_{basal} and AC_{dip} (Fig 4E). $[D2R]_{tot}$ and $[RGS]_{tot}$ were needed to fall in the overlapping region ($AC_{basal} < 30\%$, $AC_{dip} > 70\%$, and $T_{1/2} < 0.5$ s) for the DA-dip detection in LTP and/or the change of neuronal excitability (Fig 4E). As expected, this region depended on $[DA]_{basal}$ and $[DA]_{dip}$ (S5 Fig). The higher $[DA]_{basal}$ and lower $[DA]_{dip}$ were required for the dynamics range in the response of AC_{primed} , while the lower $[DA]_{basal}$ was better for the rapid response (S5A Fig, right). The requirements of the D2R–RGS balance and high $[RGS]_{tot}$ were preserved regardless of the concentrations of DA.

All the characteristics of $T_{1/2}$ were also preserved in the competitive model (Figs 4D and S4D), and $T_{1/2}$ in the competitive model further depended on the binding/unbinding reaction rate of G_{olf} (S6 Fig). This is because AC_{primed} represented the state of G_i -free and G_{olf} -bound AC, and the G_{olf} binding rate became a time limiting process if the G_{olf} binding process was slower than the G_i unbinding process. The reaction rate of G_{olf} did not affect the requirement of the D2R–RGS balance (S6A and S6B Fig, center), because it did not affect the steady-state

level of G_{olf} but the dissociation constant, $K_{d,G_{olf}}$ should affect it. Similar reaction-rate dependency has been examined by Bruce et al. (2019) [20].

Analytical formulation

The D2 model revealed that DA dip could be detected only in a restricted range in the space of $[RGS]_{tot}$ and $[D2R]_{tot}$ (Fig 3D). However, this requirement has been demonstrated only for the standard set of parameters (S1 and S2 Tables), while it should also depend on the other type of parameters, i.e., kinetic constants (S2 Table). Similarly, we defined the DA-dip detectable region, i.e., $AC_{basal} < 30\%$, $AC_{dip} > 70\%$, and $T_{1/2} < 0.5$ s, mainly for convenience, and they do not necessarily take exactly these values. We thus derived their analytical solutions to examine the overall parameter dependence of AC_{basal} and AC_{dip} , and $T_{1/2}$.

To enable it, we first made simplification on the enzymatic reactions based on the MM formulation. We introduced the catalyst-saturated approximation, $d[P]/dt \sim [E]k_{cat}$ if $K_m \ll [S]$, to the GTP/GDP exchange of G_i -GDP, i.e.,

$$(a) K_{m,exch,G_i} \ll [G_i \cdot G_{\beta\gamma}],$$

where $K_{m,exch,G_i}$ is the Michaelis constant, and $[G_i \cdot G_{\beta\gamma}]$ is the substrate concentration. The constraint (a) was based on the facts that $K_{m,exch,G_i} \sim 10$ nM (S2 Table) and $[G_i]_{tot} \sim 10$ μ M (S1 Table). Thus, in almost all the situations, $K_{m,exch,G_i}$ was much lower than $[G_i \cdot G_{\beta\gamma}]$. Similarly, we introduced the first-order rate approximation, $d[P]/dt \sim [E][S]k_{cat}/K_m$ if $K_m \gg [S]$, to the GTP hydrolysis of G_i , i.e.,

$$(b) K_{m,hyd,G_i} \gg [G_i \cdot GTP],$$

where K_{m,hyd,G_i} is the Michaelis constant, and $[G_i \cdot GTP]$ is the substrate concentration. The constraint (b) was based on the parameters that $K_{m,hyd,G_i} \sim 12$ μ M and $[G_i]_{tot} \sim 10$ μ M (S1 and S2 Tables). Only a subpopulation of $[G_i]_{tot}$ forms $[G_i \cdot GTP]$; thus, $K_{m,hyd,G_i} > [G_i]_{tot} > [G_i \cdot GTP]$, and $K_{m,hyd,G_i} > [G_i \cdot GTP]$. We further set the following constraints:

$$(c) [D2R] \cdot [DA] / [D2R:DA] = K_{d,DA}, \text{ where } K_{d,DA} = k_{off,DA}/k_{on,DA},$$

$$(d) V_7 = 0 \text{ where } V_7 = k_{on,G_iGDP}[AC_i^{site}][G_i \cdot GDP] \text{ (see section A in S1 Appendix).}$$

The constraint (c) was set because the binding of DA to D2R rapidly reaches equilibrium ($t_{1/2} \sim 30$ ms, S2 Table) [11,19], and the constraint (d) is the assumption that G_i -GDP never binds to AC, which is compatible with $K_{d,G_iGDP} \ll K_{d,G_iGDP}$ (S2 Table) [18]. Note that the constraint (d) was also assumed in the other D2 model as the simultaneous occurrence of G_i -GTP hydrolysis at the time of its detachment from AC5 [19]. Simplification of the D2 model based on the constraints (a-d) is described in section A in S1 Appendix.

Based on the constraints (a-d), we successfully obtained the steady-state ratio of G_{olf} -bound and G_i -free forms of AC, AC_{basal} and AC_{dip} , as follows (Eqs (S53) and (S61) in section B in S1 Appendix):

$$AC_{basal} = \frac{-b_{basal} + \sqrt{b_{basal}^2 - 4c_{basal}}}{2}, \tag{13}$$

$$b_{basal} = \left\{ \frac{(k_{off,G_iGTP} + k_{RGS})}{k_{on,G_iGTP}} \frac{\chi}{[AC]_{tot}} + \left(\frac{1}{k_{RGS}} + \frac{1}{k_{off,G_iGDP}} \right) \frac{[D2R]_{tot}}{[AC]_{tot}} k_{DA,basal} - 1 \right\},$$

$$c_{\text{basal}} = - \frac{(k_{\text{off,GiGTP}} + k_{\text{RGS}}) \chi}{k_{\text{on,GiGTP}} [AC]_{\text{tot}}},$$

$$\chi = \begin{cases} 1 & \text{(standard non-competitive model)} \\ 1 + G_{\text{olf}} & \text{(competitive model)} \end{cases},$$

where $k_{\text{RGS}} = k_{\text{cat,hyd,Gi}}/K_{\text{m,hyd,Gi}} \cdot [RGS]_{\text{tot}}$, $k_{\text{DA,basal}} = k_{\text{cat,exch}} [DA]_{\text{basal}} / ([DA]_{\text{basal}} + K_{\text{d,DA}})$, and $G_{\text{olf}} = [G_{\text{olf}}]_{\text{buff}}/K_{\text{d,Golf}}$ (see **S1 and S2 Tables and section B in S1 Appendix**). AC_{dip} was also obtained by replacing $k_{\text{DA,basal}}$ with $k_{\text{DA,dip}}$. The analytical AC_{basal} and AC_{dip} were both well fitted with the simulated AC_{basal} and AC_{dip} , respectively (**Figs 3B, 3C, 3D and 3AB**; blue and light-blue dotted lines), and the analytical AC_{basal} and AC_{dip} were the functions of $[RGS]_{\text{tot}}$, $[D2R]_{\text{tot}}$, and $[AC]_{\text{tot}}$, but not the function of $[G_i]_{\text{tot}}$. This is because the constraint (a) simplified the G_i -dependent V_1 (Eqs (5), (S1), and (S5), **section A in S1 Appendix**) into a G_i -independent form (Eqs (S43) and (S44), **section A in S1 Appendix**). The constraint (a), $K_{\text{m,exch,Gi}} \ll [G_i;G_{\beta\gamma}]$, was invalid in the small range of $[G_i]_{\text{tot}}$; thus, the analytical and simulated AC_{basal} were mismatched under $[G_i]_{\text{tot}} < \sim 0.04 \mu\text{M}$ (**Fig 3B**, second right).

Eq (24) well described the simulated AC_{basal} and AC_{dip} . However, even with the constraints (a–d), Eq (24) was still too complicated to provide an intuitive understanding. We thus further simplified Eq (13) by considering its asymptotic functions under $k_{\text{RGS}} \ll k_{\text{off,GiGDP}}, k_{\text{off,GiGTP}}$, i.e.,

$$[D2R]_{\text{tot}} = \frac{1 - AC_{\text{basal}}}{k_{\text{DA,basal}}} \left\{ [AC]_{\text{tot}} + K_{\text{d,GiGTP}} \frac{\chi}{AC_{\text{basal}}} \right\} k_{\text{RGS}}, \tag{14}$$

and under $k_{\text{RGS}} \gg k_{\text{off,GiGDP}}, k_{\text{off,GiGTP}}$, i.e.,

$$[D2R]_{\text{tot}} = \frac{1 - AC_{\text{basal}}}{k_{\text{DA,basal}}} k_{\text{off,GiGDP}} \left\{ [AC]_{\text{tot}} + \frac{k_{\text{RGS}}}{k_{\text{on,GiGTP}}} \frac{\chi}{AC_{\text{basal}}} \right\}. \tag{15}$$

Here, $k_{\text{RGS}} \ll k_{\text{off,GiGDP}}, k_{\text{off,GiGTP}}$ denotes the situation that G_i -GTP hydrolysis is much slower than the G_i -dissociation rate from AC, and $k_{\text{RGS}} \gg k_{\text{off,GiGDP}}, k_{\text{off,GiGTP}}$ denotes the reversed situation. Eqs (14) and (15) denote the isolines of AC_{basal} , i.e., $[D2R]_{\text{tot}} = f([RGS]_{\text{tot}}; AC_{\text{basal}})$, and they are both linear functions of $[RGS]_{\text{tot}} (\propto k_{\text{RGS}})$; thus, AC_{basal} can be characterized by a transition between the two linear functions (**Fig 5A**). The gradients and D2R-intercept depend on AC_{basal} , $[DA]_{\text{basal}}$, $[AC]_{\text{tot}}$, and kinetic constants. One of the asymptotic functions, Eq (15), appeared to be curved in the logarithmic space (**Fig 5A**, light-blue dashed line), but it is due to the D2R-intercept, and indeed linear in the linear space. The other asymptotic function (Eq (14); **Fig 5A**) appeared to be linear, because it has no D2R- or RGS-intercepts. AC_{dip} was also derived where $k_{\text{DA,basal}}$ was replaced with $k_{\text{DA,dip}}$, and showed the same characteristics (**Fig 5B**).

We next considered the half maximal time of $AC_{\text{primed}}(t)$, $T_{1/2}$, where $AC_{\text{primed}}(t = T_{1/2}) = (AC_{\text{basal}} + AC_{\text{dip}}) / 2$ after a sudden decrease of $[DA]$ at $t = 0$ s (Eq (5); **Fig 3A**). Unfortunately, the dynamics of $AC_{\text{primed}}(t)$ was governed by exponentials of exponential functions, which has a complicated form (gamma functions) in the analytical solution. To avoid it, we further introduced three additional constraints to the D2 model:

(e) $[AC_i^{\text{site}}] \cdot [G_i\text{-GTP}] / [AC_i^{\text{site}} : G_i\text{-GTP}] = K_{\text{d,GiGTP}}$,

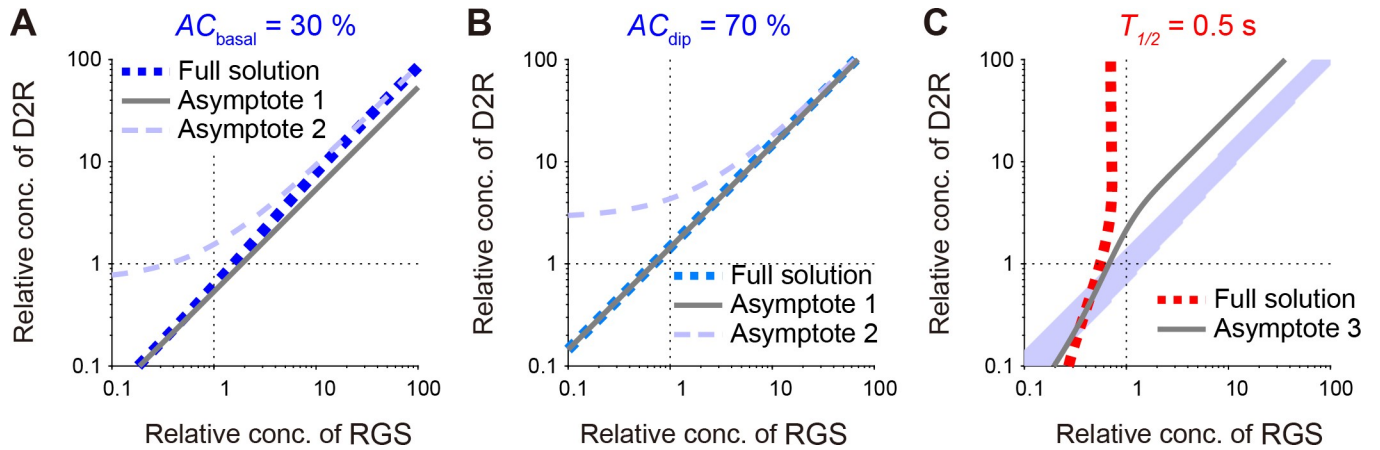


Fig 5. DA-dip detectable regions are characterized by asymptotic functions. (A, B) Analytical isolines of AC_{basal} and AC_{dip} ($AC_{basal} = 30\%$, blue dotted line; $AC_{dip} = 70\%$, light-blue dotted lines) are characterized by a transition between two linear functions, Eq (14) and Eq (15) (gray and light-blue dashed lines, respectively). (C) Analytical iso- $T_{1/2}$ line ($T_{1/2} = 0.5$ s, red dotted line) is approximated by the function Eq (19) (gray dashed line) if it is located within $AC_{basal} < 30\%$ and $AC_{dip} > 70\%$ (blue shaded area).

<https://doi.org/10.1371/journal.pcbi.1009364.g005>

$$(f) [AC_i^{site}] \cdot [G_i-GDP] / [AC_i^{site} : G_i-GDP] = K_{d,GiGDP},$$

$$(g) [AC_{olf}^{site}] \cdot [G_{olf}-GTP] / [AC_i^{site} : G_{olf}] = K_{d,Golf} \text{ (only for the competitive model),}$$

where $K_{d,GiGTP} = k_{off,GiGTP} / k_{on,GiGTP}$, $K_{d,GiGDP} = k_{off,GiGDP} / k_{on,GiGDP}$, and $K_{d,Golf} = k_{off,Golf} / k_{on,Golf}$. The constraints (e-g) assume that the AC- G_i and AC- G_{olf} bindings rapidly reach equilibrium, and the dynamics of $AC_{primed}(t)$ is governed by G_i -GTP hydrolysis. This operation is called the rapid equilibrium assumption in enzymology. We denoted AC_{primed} and $T_{1/2}$ under the constraints (e-g) as \widehat{AC}_{primed} and $\widehat{T}_{1/2}$, respectively, and $\widehat{T}_{1/2}$ was obtained as:

$$\widehat{T}_{1/2} = \frac{1}{k_{RGS}} \ln \left\{ \frac{k_{DA,basal} - k_{DA,dip}}{(1 - \widehat{AC}_{1/2}) \left\{ [AC]_{tot} + K_{d,GiGTP} \frac{\chi}{AC_{1/2}} \right\} \frac{k_{RGS}}{[D2R]_{tot}} - k_{DA,dip}} \right\}, \quad (16)$$

where $\widehat{AC}_{1/2} = (\widehat{AC}_{basal} + \widehat{AC}_{dip})/2$, and \widehat{AC}_{basal} and \widehat{AC}_{dip} were given by:

$$\widehat{AC}_{basal} = \frac{-b_{basal} + \sqrt{b_{basal}^2 - 4c_{basal}}}{2}, \quad (17)$$

$$b_{basal} = \frac{K_{d,GiGTP}}{[AC]_{tot}} \chi + \frac{[D2R]_{tot}}{[AC]_{tot}} \frac{k_{DA,basal}}{k_{RGS}} - 1,$$

$$c_{basal} = -\frac{K_{d,GiGTP}}{[AC]_{tot}} \chi,$$

$$\widehat{AC}_{dip} = \frac{-b_{dip} - \sqrt{b_{dip}^2 - 4c_{dip}}}{2}, \quad (18)$$

$$b_{dip} = \frac{K_{d,GiGTP}}{[AC]_{tot}} \chi + \frac{[D2R]_{tot}}{[AC]_{tot}} \frac{k_{DA,dip}}{k_{RGS}} - 1,$$

$$c_{dip} = -\frac{K_{d,GiGTP}}{[AC]_{tot}}\chi.$$

The derivations of Eqs (16), (17), and (18) are described in **section C in S1 Appendix**. The analytical $\hat{T}_{1/2}$ was well fitted with the simulated $T_{1/2}$ (red dotted line, **Figs 4B, 4C, 4D and S4D**), showing the validity of the analytical formulation. The constraints (e, f) are not valid if the hydrolysis rate of G_i-GTP, k_{RGS} , is much larger than the rate of AC-G_i unbinding, and this invalidity appeared in the high $[RGS]_{tot}$ (**Fig 4B**, second left). Similarly, the constraint (g) is not valid if k_{RGS} is much larger than the rate of AC-G_{oIf} unbinding, as it also appeared (**S6B Fig**, right).

We finally simplified Eq (27) by considering if $\widehat{AC}_{1/2} \rightarrow 50\%$:

$$[D2R]_{tot} = \frac{k_{RGS}}{2} \frac{[AC]_{tot} + 2\chi K_{d,GiGTP}}{(k_{DA,basal} - k_{DA,dip})\exp(-k_{RGS} \cdot \hat{T}_{1/2}) + k_{DA,dip}}. \tag{19}$$

Here, $\widehat{AC}_{1/2} \rightarrow 50\%$ represents an ideal situation, i.e., $AC_{basal} = 0\%$ and $AC_{dip} = 100\%$, or $AC_{basal} + AC_{dip} = 100\%$. The asymptotic $\hat{T}_{1/2}$ (**Fig 4C**, gray dashed line) was almost the same as the analytical one (**Fig 5C**, red dotted line) if $AC_{basal} < 30\%$ and $AC_{dip} > 70\%$ (**Fig 5C**, blue shaded area). We thus obtained an analytically closed form of the isoline of $T_{1/2}$ in the DA-dip detectable region. In Eq (19), $\hat{T}_{1/2}$ is the decreasing function of $[RGS]_{tot} (\propto k_{RGS})$. Thus, $[RGS]_{tot}$ must be higher than the isoline for the shorter DA-dip detection.

In summary, we derived the analytical forms of AC_{basal} , AC_{dip} , and $T_{1/2}$. AC_{basal} and AC_{dip} were both characterized by the transition between two asymptotic linear functions (Eqs (14) and (15); **Fig 5A and 5B**), and $T_{1/2}$ also had an approximate closed form (Eqs (16)–(18); **Fig 4B–4E**). The boundaries of AC_{basal} and AC_{dip} were linear regardless of the model parameters as far as they satisfied the constraints (a–d), and such a linear relationship was also seen in developing mice (**Fig 3E**) [28].

AC-concentration dependence

The DA-dip detectability also depended on $[AC]_{tot}$ (**Figs 3B and 4B**, center). We thus examined two-way relationships between $[AC]_{tot}$ and $[D2R]_{tot}$ (**S7C and S7F Fig**) as well as between $[AC]_{tot}$ and $[RGS]_{tot}$ (**S7D and S7G Fig**). The DA-dip detectable region in $[AC]_{tot}$ showed a positive relationship with that in $[D2R]_{tot}$ (**S7C Fig**), and a negative relationship with that in $[RGS]_{tot}$ (**S7D and S7G Fig**). These $[AC]_{tot}$ dependences originated from the sequestration of G_i-GTP for the inhibition of AC. If G_i-GTP was set not to be sequestered by AC, i.e., V_4, \dots, V_7 were removed only from Eq (S3) (**S7A and S7H Fig**), the $[AC]_{tot}$ dependences were completely eliminated (**S7J, S7K and S7N Fig**), while the relationship between $[RGS]_{tot}$ and $[D2R]_{tot}$ was still preserved (**S7I and S7L Fig**). Furthermore, the lower $[AC]_{tot}$ was, the lower $[AC]_{tot}$ dependences appeared (**S7C, S7D and S7G Fig**) because the smaller amount of G_i-GTP was sequestered by AC.

Dynamics of AC_{primed} under psychiatric/movement disorders

Healthy mice show an age-dependent simultaneous increase in the levels of striatal D2R and RGS9–2 during postnatal development (**Fig 3E**) [28,50,51]. This D2R–RGS balance is known to be disrupted in psychiatric/movement disorders. Schizophrenia patients often show a super-sensitivity of D2R and/or an increase in DA [29,60], and mice in a corresponding mouse

model show the decrease in the gross expression level of RGS9–2 in the striatum [31,32]. The altered levels of D2R and RGS disturb the intracellular signaling of SPNs [61], and such abnormal signaling and subsequent striatal dysfunction is expected to cause these psychological symptoms [62]. By contrast, a mouse model of DYT1 dystonia shows the decrease and increase in D2R and RGS9–2, respectively, in the co-existent fraction of D2R and RGS9–2 (DRM; Fig 3E, red points) [28], and the increased GTP hydrolysis may be related to involuntary movements. Thus, we explored the DA-dip detectability under such D2R–RGS imbalances (Fig 6).

We first confirmed that the D2 model with the standard set of parameters (healthy-adult model; Fig 6A, gray circle) successfully detected short DA dips (~0.5 s; Fig 6B). The AC_{primed} was sufficiently low under the steady-state G_i -GTP (Fig 6B; $AC_{\text{basal}} = 19\%$ where $[G_i\text{-GTP}]_{\text{basal}} = 0.24 \mu\text{M}$), whereas the AC_{primed} was sufficiently and rapidly increased during DA dips (Fig 6B; $AC_{\text{dip}} = 78\%$ where $[G_i\text{-GTP}]_{\text{dip}} = 0.016 \mu\text{M}$). Then we set a condition for healthy infant that had $0.5 \times [D2R]_{\text{tot}}$ and $0.5 \times [RGS]_{\text{tot}}$ (Fig 6A, green circle), and found the similar response of AC_{primed} to the DA dips (Fig 6C; $AC_{\text{basal}} = 17\%$ where $[G_i\text{-GTP}]_{\text{basal}} = 0.23 \mu\text{M}$; $AC_{\text{dip}} = 78\%$ where $[G_i\text{-GTP}]_{\text{dip}} = 0.014 \mu\text{M}$), although it showed lower sensitivity to the shorter dips. On the contrary, a schizophrenia model that had $4.0 \times [D2R]_{\text{tot}}$ and $0.5 \times [RGS]_{\text{tot}}$ (Fig 6A, blue circle) did not detect the DA dips because of the excessive amount of G_i -GTP. It caused the excessively low AC_{primed} at the basal state and its lower and slower increase (Fig 6D; $AC_{\text{basal}} = 2\%$ where $[G_i\text{-GTP}]_{\text{basal}} = 2.8 \mu\text{M}$; $AC_{\text{dip}} = 21\%$ where $[G_i\text{-GTP}]_{\text{dip}} = 0.19 \mu\text{M}$). Similarly, a dystonia model that had $0.5 \times [D2R]_{\text{tot}}$ and $2.0 \times [RGS]_{\text{tot}}$ (Fig 6A, red circle) showed high AC_{basal} and weak responses to the DA dips (Fig 6E; $AC_{\text{basal}} = 57\%$ where $[G_i\text{-GTP}]_{\text{basal}} = 0.050 \mu\text{M}$; $AC_{\text{dip}} = 94\%$ where $[G_i\text{-GTP}]_{\text{dip}} = 0.0043 \mu\text{M}$). In summary, the D2 models for healthy adult and healthy infant responded to DA dips with sufficiently large dynamic ranges (Fig 6F, gray and green lines, respectively), although the healthy-infant model was less sensitive to shorter DA dips. The schizophrenia model showed the slower and smaller responses of AC against DA dips (Fig 6F, blue line), and the dystonia model showed the rapid but small response (Fig 6F, red line).

Apparently, their DA-dip detectability was disrupted by the excessive or insufficient levels of G_i -GTP at the basal states (Fig 6B–6E, center), and they can be understood using a schematic picture (S8A Fig). At the basal state, DA-dependent D2R activity works like a faucet (tap) that provides G_i -GTP with a constant rate (S8A Fig, left). The production rate, V_1 , is almost independent of $[G_i:G_{\text{p}}]$ because $[G_i]_{\text{tot}}$ (~9 μM) is much higher than $K_{\text{m,exch,Gi}}$ (~0.01 μM , S2 Table; constraint (a)). The produced G_i -GTP is drained through RGS, where the draining rate, $V_2 + V_8$, is proportional to $[G_i\text{-GTP}] + [AC:G_i\text{-GTP}]$ (Eqs (S40) and (S41), section A in S1 Appendix) because the GTP hydrolysis is unsaturated (constraint (b)). The difference in these rates makes a pool of G_i -GTP (S8A Fig, left). In the healthy-adult model, the pooled G_i -GTP almost completely inhibits AC, which is represented by a ball (S8A Fig). Here, the G_i -soaked part of AC is inhibited, and the G_i -free part is disinhibited (S8A Fig, inset). During the DA-dip, the production of G_i -GTP almost stops (S8A Fig, right), and the level of G_i -GTP is decreased for the activation of AC for LTP and/or the change of neuronal excitability. In the schizophrenia model, the larger $[D2R]_{\text{tot}}$ makes the production rate of G_i -GTP, V_1 , much higher than its draining rate, $V_2 + V_8$ (S8D Fig), leading to the complete inhibition of AC. In the dystonia model, the production rate is conversely lower than the draining rate (S8E Fig). These imbalances caused the decrease the levels of DA-dip detection (Fig 6F).

Time windows for AC_{active} under psychiatric/movement disorders

Finally, we examined the timing detection for AC1 in D2 SPNs in the healthy adult, healthy infant, schizophrenia, and DYT1 dystonia (Fig 7). Compared to the healthy-adult model (the

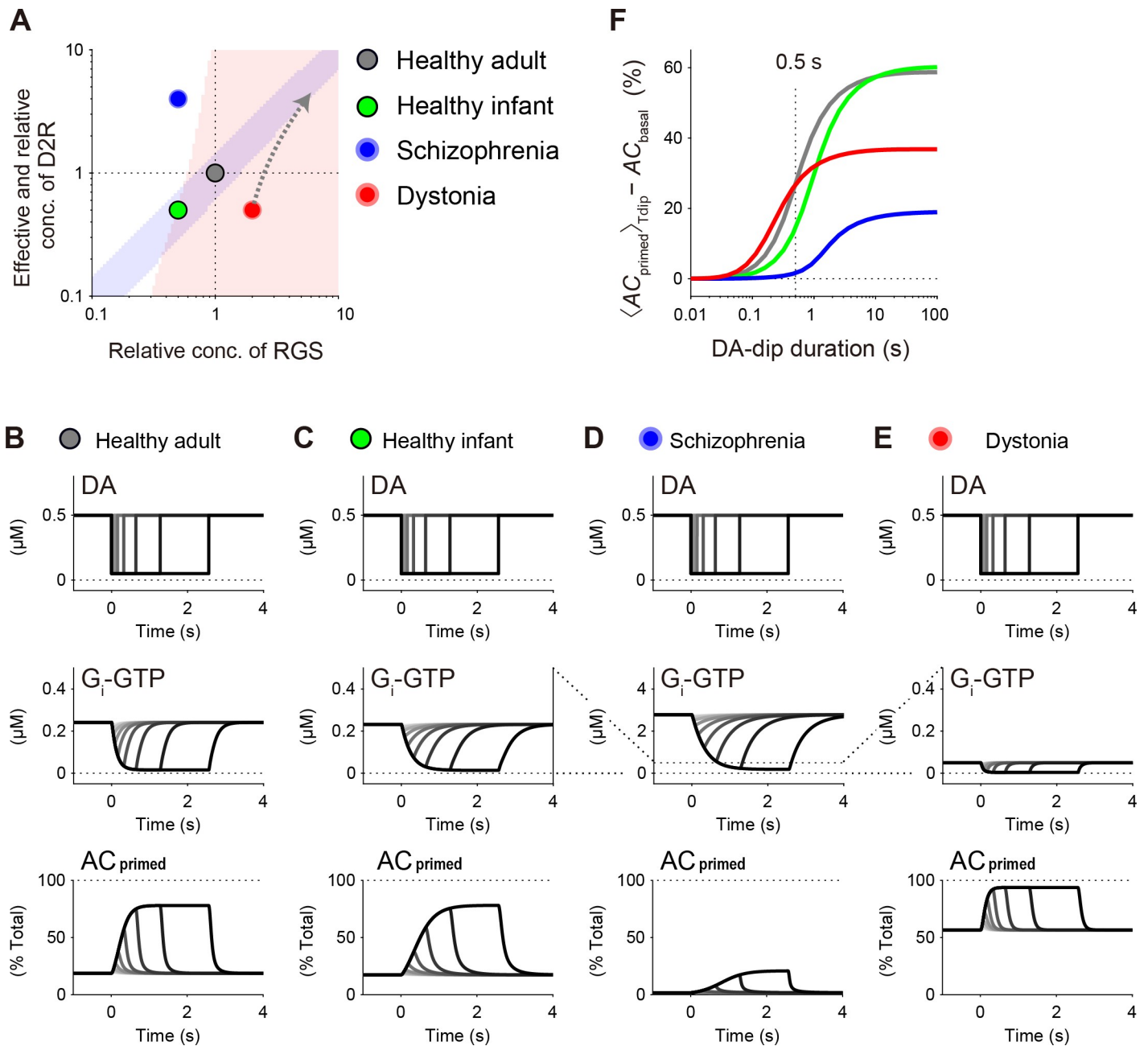


Fig 6. DA dip is undetectable under the pathologic imbalance between D2R and RGS. (A) Levels of D2R and RGS under healthy and pathologic conditions. Healthy infant mice show lower levels of D2R and RGS (green circle) than healthy adult mice do (standard model; gray circle, see Fig 2D) [28]. Schizophrenia patients are known to show higher and lower activities of D2R and RGS, respectively (blue circle) [29,31,32], and a mouse model of DYT1 dystonia shows the opposite changes in their levels (red circle, Fig 2D) [28]. Gray arrow denotes the hypothetical trajectory of changes in RGS and D2R levels if the levels of RGS and D2R are increased from the dystonic levels by the same ratio as in the increasing ratio under the development of healthy mice, i.e., $([D2R], [RGS]) = \mu \times ([D2R]_{\text{tot}}, [RGS]_{\text{tot}}) + ([D2R]_{\text{Dystonia}}, [RGS]_{\text{Dystonia}})$ where $[D2R]_{\text{Dystonia}}$ and $[RGS]_{\text{Dystonia}}$ are the dystonic levels of D2R and RGS, and μ is the constant (> 0 ; see Discussion). (B–E) Dynamics of $[G_i\text{-GTP}]$ and AC_{primed} against DA dips with a variety of durations (0.01 s, 0.02 s, ..., 2.56 s). (F) Summary of the DA-dip duration dependences quantified using $\langle AC_{\text{primed}} \rangle_{\text{Tdip}} - AC_{\text{basal}}$ (see Methods).

<https://doi.org/10.1371/journal.pcbi.1009364.g006>

standard set of parameters, S1 and S2 Tables and Fig 7A), the healthy-infant model showed the smaller level of DA-dip detection in AC_{active} because the DA dips had a short period of 0.5 s (Fig 7B). The schizophrenia model did not show any increase in AC_{active} (Fig 7C), while the

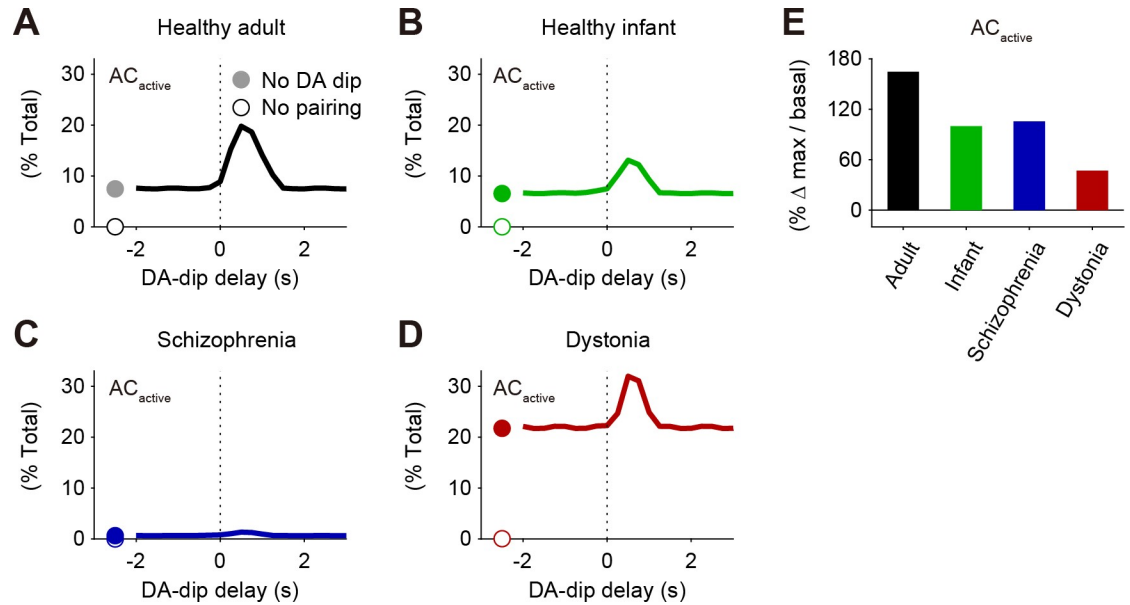


Fig 7. Decreased efficacy of the coincidence detection in pathologic/movement disorders. (A–D) Time windows for DA-dip delay against pre–post pairing on the activity of AC1, $[AC_{active}]$, in the models of healthy adult (A), healthy infant (B), schizophrenia (C), and DYT1 dystonia (D). For each DA-dip delay, a 0.5-s DA dip is paired with 1-s pre–post pairing. Obtained maximal $[AC_{active}]$ are normalized by the total concentrations of AC1, $[AC]_{tot}$. (E) Maximal amplitudes of AC_{active} normalized by the basal level.

<https://doi.org/10.1371/journal.pcbi.1009364.g007>

dystonia model detected the DA-dip, but the timing-independent component of AC_{active} was high (Fig 7D). Because of the high timing-independent AC_{active} , the peak-to-basal ratio of AC_{active} in the DYT1 dystonia became the lowest (Fig 7E), indicating the small signal-to-noise ratio even if the activity of the downstream signaling can adapt to the high timing-independent levels of AC_{active} .

Following a previous study [24], we also simulated AC5 coincidence detection between a phasic burst of adenosine (duration: 1 s) and a DA dip/burst (duration: 2 s; S9A–S9C Fig). The time windows for the delay of DA dip/burst were similar to those in AC1 (S9D–S9G Fig), and the dystonia model rather showed DA-burst detection, because the longer DA burst completely inhibited the increase in AC_{active} due to the adenosine burst (S9G Fig, thin lines).

Discussion

Here, we showed that a D2R–RGS balance was required for the detection of DA dips in D2 SPNs, where the DA-dip detection is important for the LTP and/or change of neuronal excitability. High-level RGS was further required for the detection of short (~0.5 s) DA dips. These requirements were satisfied in healthy development but disrupted in our models of schizophrenia and DYT1 dystonia.

The D2 model highlights the importance of RGS. In particular, a type of RGS, RGS9–2, is known to be specifically and abundantly expressed in the striatum [27,34,63]. The expression of RGS9–2 is co-regulated with that of D2R [28,64], and RGS9–2 itself is associated and colocalized with D2R [65]. The present study provides a reason why RGS9–2 is so tightly coupled with D2R. It is necessary for the reliable detection of short DA dips. The abundance of RGS9 is also seen in the retinal phototransduction processes [66], and the rapid hydrolysis of transduction via RGS9 is vital for the rapid visual processing both in rods and cones [67]. Although G-protein signaling is often discussed from its chronic aspects [68], it can also serve for sub-second information processing. In addition, a variety of RGS subtypes are expressed in the brain

in a region-specific manner [63,69]. RGS8 and RGS10 are characteristically expressed in cerebellar Purkinje cells as well as in the stratum granulosum of the hippocampus, respectively [63]. They may also play roles for region-specific information processing.

Nair et al. have already demonstrated DA-dip detection by AC5 in the model of D2 SPNs [19,24], in which a set of model parameters were determined based on observed molecular activities. The D2 signaling model has shown the requirement of a longer DA dip for the AC5 response (c.f., Fig 6) [19]. It has also shown the requirement of higher concentration of basal DA for the AC5 response, which was shown as the region of $AC_{\text{basal}} < 30\%$ in the D2 model (S5A Fig, left). Further, the D2 signaling model has shown the requirement of lower concentration of DA during a DA dip [24], as shown in $AC_{\text{dip}} > 70\%$ of the D2 model (S5B Fig, left). However, the D2 signaling model does not incorporate RGS, but the GTP hydrolysis of G_i is assumed to occur with a constant rate. Here, we extensively examined the concentration dependence of five target molecules (Fig 3B), and found the requirement of the D2R–RGS balance for the DA dip detection, together with the analytical solutions that prove the universality of the balance requirement. Nair et al. have also demonstrated a possible coincidence detection between DA thirst and acetylcholine (ACh) dip, the latter of which leads to the deactivation of a G_i -coupled receptor (muscarinic M4 ACh receptor; M4R) [24]. RGS should also play a critical role in such other types of G_i inactivation-driven events.

In the present study, we derived analytical solutions for the DA-dip detection. They were valid in a wide range of parameters, as far as the D2 model satisfied the constraints (a–g). In particular, the constraints (a, b) were related to famous simplifications of the MM formulation. The constraint (a) enabled the catalyst-saturated approximation, and the constraint (b) enabled the first-order rate approximation. They contributed not only to the simplification but also to stable DA-dip detection. For example, if the G_i -GTP hydrolysis were conversely saturated, the GTP hydrolysis rate, $V_2 + V_8$ (Eq (S65) in section C in S1 Appendix), would be independent of $[GTP]$ ($= [G_i-GTP] + [AC:G_i-GTP]$), but only dependent on $[RGS]$. Then, $[GTP]$ would become an increasing or decreasing function depending only on $[RGS]$, and G_i took only one of two stable states, i.e., fully hydrolyzed or non-hydrolyzed states. AC_{primed} could not show a rapid increase from the fully non-hydrolyzed state of G_i (i.e., 100% G_i -GTP), nor detect a short DA-dip. The kinetics constants and molecular concentrations seem to be arranged for effective DA-dip detection, which may be a design principle in the biological system, as often quoted in the field of systems biology [70].

In schizophrenia, the balance between D2R and RGS activities is considered to be biased toward D2R (Fig 6A), because D2R blockers works as antipsychotic drugs for schizophrenia [52,53], and schizophrenia shows show a supersensitivity of D2R and/or an increase in striatal DA [29,60] as well as a decrease in striatal RGS9–2 [31,32]. Our D2 model predicts that the excessive activity of postsynaptic D2R completely inhibits AC, disabling the detection of any DA dips as well as subsequent LTP (Fig 7C). Correspondingly, chronic upregulation of D2R is known to result in the rewiring of connections first from the striatum to the globus pallidus (GPe) [71] and next within the frontal cortex [61,62]. Such rewiring may lead to the persistent symptoms of schizophrenia. D2R blockers are widely used for the medication of schizophrenia [52], but the present study predicts that the excess blockage of D2R again disables DA-dip detection. Indeed, excessive treatment with the D2R blockers is known to induce extrapyramidal side effects including tardive dyskinesia [31,72], a movement disorder that shares the similar symptoms with DYT1 dystonia [73] whose mouse model shows the D2R–RGS imbalance toward RGS (Fig 2D).

DYT1 dystonia is a hyperkinetic movement disorder, which originates from a Δ gag mutation in the *TOR1A* gene. It decreases the gross expression levels of both D2R and RGS9–2 [73,74], but the level of RGS9–2 is selectively increased in the DRM where D2R is located, and

the D2R–RGS balance is biased toward RGS. In our D2 model, the excess RGS first decreases the level of G_i -GTP, and then increases the AC activity for cAMP production. Excess cAMP is expected to be a cause of abnormal LTP [33,54,75,76]. Such synaptic abnormality leads to the abnormal neuronal activities in GPe [77] and thalamus [78], and they may cause muscle contractions and irregular tremors [79]. Notwithstanding with these reports, DA drugs do not provide clinical benefit [80], and the viral overexpression of RGS9–2 rather restores normal neuronal electrophysiology [28]. These inconsistent observations are reconciled in the scheme of the D2 model as follows. First, DA drugs should not work because they cannot accurately control the level of D2R activity to counteract with RGS (Fig 6A). Next, the overexpression of RGS9–2 also rescues the decreased expression level of D2R [28], and the increased levels of RGS and D2R can be balanced within the DA-dip detectable region. Indeed, this rebalancing would be realized if the levels of RGS and D2R were increased from the dystonic levels by the same ratio as in normal development (Fig 6A, gray arrow). The overexpression of RGS9–2 thus can restore normal neuronal activity [28]. Together, the D2 model explains many aspects of DYT1 dystonia in the space of D2R and RGS, including the aspects of healthy development and schizophrenia.

The balance requirement between D2R and RGS itself has been recognized in the field of psychiatry [32,53], and here we re-formalized it as requirements for the DA-dip detection for LTP in D2 SPNs. Note that pairs of $[D2R]_{tot}$ and $[RGS]_{tot}$ for the healthy and pathologic conditions were determined only for exemplifying purpose (Fig 6A), and their absolute values are case-dependent even in mice experiments (see Methods). In particular, schizophrenia is caused by both environmental and genetic factors, and many combinations of the genes affect schizophrenia [81]. Thus, the pairs of effective $[D2R]_{tot}$ and $[RGS]_{tot}$ are expected to span a wide range depending on the patients, even if it is caused by excessive D2R activity.

The other major movement disorder, L-DOPA induced dyskinesia (LID), could also be related to the D2R–RGS imbalance. The depletion of DA is associated with Parkinson's disease, and the DA depletion is restored by administration of a DA precursor, L-DOPA [82]. The L-DOPA medication leads to varying levels of basal DA, which is followed by the co-adaptation of D2R and RGS9–2 [28,65]. The incompleteness of the adaptation may be a cause of LID. Indeed, RGS9–2 knock-out (KO) develops LID [65], and the overexpression of RGS9–2 diminishes its involuntary movements [35]. LID also shows abnormal LTP [13,83]. However, other recent studies have shown that LID are primarily linked to the abnormal activity of D1 SPNs [84–86], and the dissection of mixed effects is necessary to understand this currently untreatable disease.

In the present study, we showed the D2R–RGS balance as a shared requirement of both AC1 and AC5. As it is known, AC5 constitutes ~80% of the total cAMP levels in SPNs [17], and contributes to synaptic plasticity [21]. Considering its abundance, AC5 should also perform the coincidence detection in some forms of synaptic plasticity as well as the plastic changes in neuronal excitability [22,23]. The AC5 coincidence detection is predicted to occur between G_{olf} and G_i (S8 Fig) [20,24]. However, in our primary target experiment, an AC1-specific inhibitor fully suppressed AC-dependent cAMP signaling, and DA signal alone did not activate the D1R– G_{olf} –AC–cAMP signaling, but further pre–post pairing (presumably Ca^{2+}) was required for the cAMP signal [5]. These observations support the role of Ca^{2+} -sensitive AC1, and further, the AC1-based D2 LTP model successfully predicted the narrow time window (~2 s) (Fig 1A) [10]. Such Ca^{2+} -sensitive ACs have been known as a coincidence detector for the classical conditioning in *Aplysia* and *Drosophila* [15,87–89]; thus, the Ca^{2+} requirement may be evolutionarily conserved [90]. The cause of missing AC5 signal in the target experiment is unknown [5], while an AC5-based model predicts much longer time window

(~10 s) [91]. In general, the expression of AC1 in the striatum is known to be decreased with the development, while the Ca^{2+} -CaM-dependent activity of AC persists [92].

AC1 and AC5 are both expressed in the cortex and hippocampus [16]. However, these regions only show weak DA signal because of the small numbers of DA fibers [93,94], and the DA signal likely plays more modulatory roles with longer time constants (~10 min) [6,95]. Rather, in these brain regions, adenosine can show persistent and transient signals with a time range of ~5 s [96,97]. Adenosine A1 receptors (A1AR) then produce $G_{i/o}$ -GTP, while A2AR produce $G_{s/olf}$ -GTP [98,99]. Thus, adenosine dip may lead to the reduction of $G_{i/o}$ -GTP via A1AR, similarly to the DA-dip signal through D2R. In the striatum, cholinergic interneurons also show tonic and ~0.1-s phasic activities [100], and the ACh release stimulates postsynaptic M4R in D1 SPNs for G_i -GTP [20,24,101]. The produced G_i -GTP may also activate AC, similar to DA-dip signal. Further, DA and ACh signals are known to interact with each other. The activity of DA fibers modulates the activity of cholinergic interneurons via co-released glutamate [102–104], and ACh conversely stimulates the DA fibers [105]. The ACh–DA interaction may enhance the coincidence detection *in vivo* [106].

An important limitation of the current D2 model is the mass assumption. In addition to well-known dimerization of D2R and A2AR [107], recent experiments have suggested that AC5, G_i , and G_{olf} also participate in the formation of a macromolecular complex that accelerated reactions among the constituents [108,109]. Such a macromolecular complex no longer obeys the mass assumption; thus, their reactions cannot be formulated by Eqs (1) and (2), but should be described in a more mechanistic manner. In the macromolecular complex, the DA signal would be more rapidly and directly transferred to the activity of AC, the short DA-dip might be more easily detected by AC. This is an attractive scenario and an important direction for future studies. Nevertheless, the D2 model should first be built based on the mass assumption, especially before the validation of its dominance in the physiological condition. As an example, the D2R: G_i : $G_{\beta\gamma}$ pre-coupled complex has been discovered and examined [110–112], but it seems not to be dominant in the physiological condition, from the viewpoint of the affinity of D2R for DA ($K_{d,DA}$ in pre-coupled complex, 25 nM; $K_{d,DA}$ in the physiological condition, ~10 μM) [1,19,43,113,114]. In addition, even if such a macromolecular complex is found to work dominantly, the current D2 model will serve as a good reference.

The present study has addressed the DA-dip detection in D2 SPNs. Similarly, phasic DA bursts are known to trigger LTP in D1 SPNs [5]. Yet, do the similar requirements exist in D1 SPNs? In D1 SPNs, DA binds to D1R, and the DA-bound D1R produces G_{olf} -GTP. However, it is known that the hydrolysis of G_{olf} -GTP is not mediated by any of the RGS, but occurs in an autocatalytic manner [46]; thus, we cannot ask the same question about D1 SPNs. Instead, we can raise another important question: how can the phasic bursts of DA trigger LTP in D1 SPNs, despite the fact that the basal DA signal alone does not trigger the LTP [1]? This question implies the existence of an adaptation mechanism for basal DA signal. A possible candidate is a feedback loop that involves a specific phosphorylation of D1R [115]. The DA-bound D1R produces G_{olf} -GTP, which activates AC. The activated AC produces cAMP and then the active form of PKA. The PKA in turn phosphorylates D1R, leading to a ~100-fold decrease in the activity of D1R, with a time constant of ~10 min [115]. Thus, the D1R–AC–PKA signaling constitutes a negative feedback loop in which D1R responds solely to the phasic DA signal. Simulation of such a feedback loop will address the stability of D1 SPNs against the fluctuation of basal DA signal. However, it requires a different model with a different level of abstraction. Thus, this topic should be addressed in other future studies.

Supporting information

S1 Fig. Schematic of the D2 model (standard non-competitive model). Arrows denote the first order reactions or enzymatic reactions, and their fluxes are denoted by V_1, \dots, V_{12} . (A) Reactions of the D2R–G_i–AC part. The input DA (circled) first regulates a G_i-protein cycle (top), then G_i-AC binding cycle (bottom). G_i-GTP/ G_i-GDP binds to a specific site of AC (AC_i^{site}). (B) Under the scheme of non-competitive binding, G_{olf}, G_i, and Ca²⁺-CaM independently interact with their specific sites of AC (AC_{olf}^{site} , AC_i^{site} , and AC_{CaM}^{site} , respectively). Simultaneous binding of G_{olf} and Ca²⁺-CaM is required for the activity of AC1 (top), and the binding of G_{olf} alone leads to the activity of AC5 (bottom). The binding of G_i inhibits the activities of both AC1 and AC5. Reactions with dashed arrows are the same as the reactions V_4, \dots, V_7 indicated in panel A.

(TIF)

S2 Fig. Schematic of the D2 model (Competitive model). Arrows denote the first order reactions or enzymatic reactions, and their fluxes are denoted by V_1, \dots, V_{20} . (A) Reactions of the D2R–G_i–AC part. Same as S1A Fig, but the G_i binding to AC disables the binding of G_{olf} and Ca²⁺-CaM. (B) If AC is free from G_i, the AC can interact with G_{olf} and Ca²⁺-CaM. Simultaneous binding of G_{olf} and Ca²⁺-CaM is required for the activity of AC1 (top), and the binding of G_{olf} alone sufficiently activates AC5 (bottom). Under the competitive binding, AC_{primed} corresponds to the levels of yellow-bordered states. Reactions with dashed arrows are the same as the reactions V_4, \dots, V_7 indicated in panel A.

(TIF)

S3 Fig. Dynamics of molecular activities in response to a DA dip. Red arrows denote the onset of a 1-s DA dip. (A) Observed molecules. (B) Optogenetically-evoked dynamics of DA. (C–I) Subsequent molecular activities. (J) Square-drop signal as a representative of DA dip. (K–Q) Subsequent molecular activities.

(TIF)

S4 Fig. DA-dip detectable region in the competitive model. (A) AC_{primed} is observed under the stepwise decreasing signal of DA. (B) Concentration dependence of the steady state levels of AC_{primed} , AC_{basal} and AC_{dip} in the competitive model. (C) G_{olf}-dependence of $\Delta AC_{activity}$ in the non-competitive and competitive models (see Eqs (7) and (10)). $\Delta AC_{active} =$

$AC_{active} |_{[DA]=[DA]_{dip}} - AC_{active} |_{[DA]=[DA]_{basal}}$ where $AC_{active} |_{[DA]=[DA]_{basal}}$ and $AC_{active} |_{[DA]=[DA]_{dip}}$ denote the activities of AC5 under $[DA]_{basal}$ and $[DA]_{dip}$, respectively. The biphasic G_{olf} concentration dependence appears only in the competitive model, as shown in Bruce et al. (2019) [20]. (D) Parameter dependence of $T_{1/2}$ in the competitive model.

(TIF)

S5 Fig. Requirement of D2R–RGS balance under various levels of $[DA]_{basal}$ and $[DA]_{dip}$. (A) $[DA]_{basal}$ is set to be 0.125, 0.25, \dots , 4 μ M (left), and the areas of $AC_{basal} < 30\%$ (top) and $T_{1/2} < 0.5$ s (bottom) are plotted in the space of $[RGS]_{tot}$ and $[DA]_{tot}$. Dotted lines denote the analytical solutions, and colored areas denote the simulation results. (B) $[DA]_{dip}$ is set to be 0.0125, 0.025, \dots , 0.4 μ M (left), and the areas of $AC_{dip} > 70\%$ (top) and $T_{1/2} < 0.5$ s (bottom) are plotted.

(TIF)

S6 Fig. Reaction rate of G_{olf} affects $T_{1/2}$ only in the competitive model. Here, the binding/unbinding reaction rate of G_{olf}, $\tau = 1/(k_{on,Golf}[G_{olf}]_{buff} + k_{off,Golf})$, is subjected to change, whereas $K_{d,Golf} (= k_{off,Golf} / k_{on,Golf})$ and $[G_{olf}]_{buff}$ are kept constant. (A, B) AC_{basal} , AC_{dip} , and

$T_{1/2}$ in the standard non-competitive model (A), and competitive model (B). Green dotted line in panel B denotes $\tau = 0.5/\log 2$ ($T_{1/2} = 0.5$ s).

(TIF)

S7 Fig. AC-concentration dependence is based on the sequestration of G_i by AC. (A–G) Areas of $AC_{\text{basal}} < 30\%$ (blue), $AC_{\text{dip}} > 70\%$ (light blue), and $T_{1/2} < 0.5$ s (pink) in the standard non-competitive model (A). These areas are plotted in the spaces of $[D2R]_{\text{tot}}$ versus $[RGS]_{\text{tot}}$ (B, E), $[D2R]_{\text{tot}}$ versus $[AC]_{\text{tot}}$ (C, F), and $[RGS]_{\text{tot}}$ versus $[AC]_{\text{tot}}$ (D, G). Dotted lines denote their analytical solutions. (H–N) Same as panels A–G, but the standard D2 model is modified so that AC sequesters G_i , i.e., V_4 , V_5 , V_6 , and V_7 are removed only from Eq (S3) but not from Eq (S12).

(TIF)

S8 Fig. Schematic of the D2-model dynamics. (A) At the steady state (left), DA-bound D2R provides a constant flux of G_i -GTP (V_1 ; see **section A in S1 Appendix**), while the G_i -GTP is drained through RGS with a speed ($V_2 + V_8$) that is proportional to the amount of G_i -GTP. Difference in the fluxes generates a pool of G_i -GTP that inhibits AC, which is represented by a sunk ball (AC). During the period of a DA dip (right), the supply of G_i -GTP nearly completely stops, and the pooled G_i -GTP is drained rapidly. AC is then disinhibited to be activated by G_{olf} and Ca^{2+} -CaM. (B–E) The G_i inhibition of AC in the healthy adult, healthy infant, schizophrenia, and dystonia, all of which are described in **Fig 6A–6E**. (C) In the healthy-infant model, the influx and efflux of G_i -GTP are both small, and the smaller efflux causes delayed disinhibition of AC during a DA dip. (D) In the schizophrenia model, hyperactive D2R provides a larger amount of G_i -GTP, thus AC is fully inhibited and its disinhibition is delayed. (E) The larger efflux of G_i -GTP in the dystonia model results in the chronic activity of AC.

(TIF)

S9 Fig. AC5 performs the coincidence detection between G_{olf} and G_i . A transient burst in adenosine (thus G_{olf}) coincides with a DA dip/burst with a variety of delay times. (A) Schematic of AC5 signaling. (B) Adenosine burst as a square wave of G_{olf} (basal, 0.16 μM ; burst, 0.8 μM ; duration, 1 s). (C) Square-wave dip and burst of DA (basal, 0.5 μM ; dip, 0.05 μM ; burst, 2 μM ; duration, 2 s). (D–G) Example traces of the AC5 activities (AC_{active} ; top), and DA-dip/burst delay dependence of the maximal AC_{active} (bottom) in the healthy-adult, healthy-infant, schizophrenia, and dystonia models. In the example traces, adenosine and DA signals were given during the periods indicated by blue and red bars, respectively. Similar simulation (adenosine versus transient DA dips) has been conducted by Nair et al. (2015) [24].

(TIF)

S1 Table. Molecular concentrations. Densities of membrane molecules should have the unit of membrane area ($/\mu\text{m}^2$), but not volume (μM). However, many of the referenced experiments/simulations have described them under homogenate conditions; therefore, we also adopted volume concentration for consistency. Note that $X_{\text{area}} / \mu\text{m}^2 \sim X_{\text{volume}} \mu\text{M} \times 20$, because a spherical spine with a radius $r_{\text{spine}} \sim 0.1 \mu\text{m}$ has the number of surface molecules $X_{\text{area}} \times (4\pi r_{\text{spine}}^2)$, and the number of cytosolic molecules is $X_{\text{volume}} \times 10^{-6} N_A \times [4\pi r_{\text{spine}}^3 / 3 \times 10^{-15}]$ where $N_A = 6.02 \times 10^{23}$ (Avogadro constant).

(PDF)

S2 Table. Reaction rate constants.

(PDF)

S1 Appendix. Model definition and analytical derivations. (A) Definition of the D2 model. (B) Derivation of analytical AC_{basal} and AC_{dip} . (C) Derivation of analytical $T_{1/2}$. (PDF)

Acknowledgments

We would like to thank Yasuo Kawaguchi and Kouichi C. Nakamura for their helpful comments, and Neruko Hayami for her support of drawing a schematic picture ([S8 Fig](#)).

Author Contributions

Conceptualization: Hidetoshi Urakubo.

Funding acquisition: Hidetoshi Urakubo, Haruo Kasai, Yoshiyuki Kubota, Shin Ishii.

Investigation: Hidetoshi Urakubo.

Resources: Sho Yagishita.

Supervision: Sho Yagishita, Haruo Kasai, Yoshiyuki Kubota, Shin Ishii.

Writing – original draft: Hidetoshi Urakubo.

Writing – review & editing: Sho Yagishita, Haruo Kasai, Yoshiyuki Kubota, Shin Ishii.

References

1. Iino Y, Sawada T, Yamaguchi K, Tajiri M, Ishii S, Kasai H, et al. Dopamine D2 receptors in discrimination learning and spine enlargement. *Nature*. 2020; 579(7800): 555–560. Epub 2020/03/28. <https://doi.org/10.1038/s41586-020-2115-1> PMID: 32214250.
2. Forsyth JK, Lewis DA. Mapping the Consequences of Impaired Synaptic Plasticity in Schizophrenia through Development: An Integrative Model for Diverse Clinical Features. *Trends Cogn Sci*. 2017; 21(10): 760–778. Epub 2017/07/30. <https://doi.org/10.1016/j.tics.2017.06.006> PMID: 28754595.
3. Schultz W. Multiple dopamine functions at different time courses. *Annu Rev Neurosci*. 2007; 30: 259–288. <https://doi.org/10.1146/annurev.neuro.28.061604.135722> PMID: 17600522.
4. Eshel N, Tian J, Bukwich M, Uchida N. Dopamine neurons share common response function for reward prediction error. *Nat Neurosci*. 2016; 19(3): 479–486. <https://doi.org/10.1038/nn.4239> PMID: 26854803.
5. Yagishita S, Hayashi-Takagi A, Ellis-Davies GCR, Urakubo H, Ishii S, Kasai H. A critical time window for dopamine actions on the structural plasticity of dendritic spines. *Science*. 2014; 345(6204): 1616–1620. ISI:000342164500047. <https://doi.org/10.1126/science.1255514> PMID: 25258080
6. Brzosko Z, Schultz W, Paulsen O. Retroactive modulation of spike timing-dependent plasticity by dopamine. *Elife*. 2015; 4. <https://doi.org/10.7554/eLife.09685> PMID: 26516682.
7. Fisher SD, Robertson PB, Black MJ, Redgrave P, Sagar MA, Abraham WC, et al. Reinforcement determines the timing dependence of corticostriatal synaptic plasticity in vivo. *Nat Commun*. 2017; 8(1): 334. <https://doi.org/10.1038/s41467-017-00394-x> PMID: 28839128.
8. Shindou T, Shindou M, Watanabe S, Wickens J. A silent eligibility trace enables dopamine-dependent synaptic plasticity for reinforcement learning in the mouse striatum. *Eur J Neurosci*. 2019; 49(5): 726–736. <https://doi.org/10.1111/ejn.13921> PMID: 29603470.
9. Kasai H, Ziv NE, Okazaki H, Yagishita S, Toyozumi T. Spine dynamics in the brain, mental disorders and artificial neural networks. *Nat Rev Neurosci*. 2021; 22(7): 407–422. Epub 2021/05/30. <https://doi.org/10.1038/s41583-021-00467-3> PMID: 34050339.
10. Urakubo H, Yagishita S, Kasai H, Ishii S. Signaling models for dopamine-dependent temporal contiguity in striatal synaptic plasticity. *PLoS Comput Biol*. 2020; 16(7): e1008078. Epub 2020/07/24. <https://doi.org/10.1371/journal.pcbi.1008078> PMID: 32701987.
11. Lohse MJ, Nikolaev VO, Hein P, Hoffmann C, Vilardaga JP, Bunemann M. Optical techniques to analyze real-time activation and signaling of G-protein-coupled receptors. *Trends Pharmacol Sci*. 2008; 29(3): 159–165. Epub 2008/02/12. <https://doi.org/10.1016/j.tips.2007.12.002> PMID: 18262662.

12. Noble EP. D2 dopamine receptor gene in psychiatric and neurologic disorders and its phenotypes. *Am J Med Genet B Neuropsychiatr Genet.* 2003; 116B(1): 103–125. Epub 2002/12/24. <https://doi.org/10.1002/ajmg.b.10005> PMID: 12497624.
13. Calabresi P, Standaert DG. Dystonia and levodopa-induced dyskinesias in Parkinson's disease: Is there a connection? *Neurobiol Dis.* 2019; 132: 104579. Epub 2019/08/25. <https://doi.org/10.1016/j.nbd.2019.104579> PMID: 31445160.
14. Wayman GA, Impey S, Wu Z, Kindsvogel W, Prichard L, Storm DR. Synergistic activation of the type I adenylyl cyclase by Ca^{2+} and G_{α} -coupled receptors in vivo. *J Biol Chem.* 1994; 269(41): 25400–25405. Epub 1994/10/14. PMID: 7929237.
15. Ferguson GD, Storm DR. Why calcium-stimulated adenylyl cyclases? *Physiology (Bethesda).* 2004; 19: 271–276. Epub 2004/09/24. <https://doi.org/10.1152/physiol.00010.2004> PMID: 15381755.
16. Visel A, Alvarez-Bolado G, Thaller C, Eichele G. Comprehensive analysis of the expression patterns of the adenylate cyclase gene family in the developing and adult mouse brain. *J Comp Neurol.* 2006; 496(5): 684–697. <https://doi.org/10.1002/cne.20953> PMID: 16615126.
17. Lee KW, Hong JH, Choi IY, Che Y, Lee JK, Yang SD, et al. Impaired D2 dopamine receptor function in mice lacking type 5 adenylyl cyclase. *J Neurosci.* 2002; 22(18): 7931–7940. <https://doi.org/10.1523/JNEUROSCI.22-18-07931.2002> PMID: 12223546.
18. Taussig R, Tang WJ, Hepler JR, Gilman AG. Distinct patterns of bidirectional regulation of mammalian adenylyl cyclases. *J Biol Chem.* 1994; 269(8): 6093–6100. PMID: 8119955.
19. Yapo C, Nair AG, Clement L, Castro LR, Helligren Kotaleski J, Vincent P. Detection of phasic dopamine by D1 and D2 striatal medium spiny neurons. *J Physiol.* 2017; 595(24): 7451–7475. <https://doi.org/10.1113/JP274475> PMID: 28782235.
20. Bruce NJ, Narzi D, Trpevski D, van Keulen SC, Nair AG, Rothlisberger U, et al. Regulation of adenylyl cyclase 5 in striatal neurons confers the ability to detect coincident neuromodulatory signals. *PLoS Comput Biol.* 2019; 15(10): e1007382. Epub 2019/10/31. <https://doi.org/10.1371/journal.pcbi.1007382> PMID: 31665146.
21. Kheirbek MA, Britt JP, Beeler JA, Ishikawa Y, McGehee DS, Zhuang X. Adenylyl cyclase type 5 contributes to corticostriatal plasticity and striatum-dependent learning. *J Neurosci.* 2009; 29(39): 12115–12124. <https://doi.org/10.1523/JNEUROSCI.3343-09.2009> PMID: 19793969.
22. Nicola SM, Surmeier J, Malenka RC. Dopaminergic modulation of neuronal excitability in the striatum and nucleus accumbens. *Annu Rev Neurosci.* 2000; 23: 185–215. Epub 2000/06/09. <https://doi.org/10.1146/annurev.neuro.23.1.185> PMID: 10845063.
23. Lahiri AK, Bevan MD. Dopaminergic Transmission Rapidly and Persistently Enhances Excitability of D1 Receptor-Expressing Striatal Projection Neurons. *Neuron.* 2020; 106(2): 277–290 e276. Epub 2020/02/23. <https://doi.org/10.1016/j.neuron.2020.01.028> PMID: 32075716.
24. Nair AG, Gutierrez-Arenas O, Eriksson O, Vincent P, Helligren Kotaleski J. Sensing Positive versus Negative Reward Signals through Adenylyl Cyclase-Coupled GPCRs in Direct and Indirect Pathway Striatal Medium Spiny Neurons. *J Neurosci.* 2015; 35(41): 14017–14030. <https://doi.org/10.1523/JNEUROSCI.0730-15.2015> PMID: 26468202.
25. Carter AG, Sabatini BL. State-dependent calcium signaling in dendritic spines of striatal medium spiny neurons. *Neuron.* 2004; 44(3): 483–493. ISI:000224771700010. <https://doi.org/10.1016/j.neuron.2004.10.013> PMID: 15504328
26. Aldridge BB, Burke JM, Lauffenburger DA, Sorger PK. Physicochemical modelling of cell signalling pathways. *Nat Cell Biol.* 2006; 8(11): 1195–1203. Epub 2006/10/25. <https://doi.org/10.1038/ncb1497> PMID: 17060902.
27. Traynor JR, Terzi D, Caldarone BJ, Zachariou V. RGS9-2: probing an intracellular modulator of behavior as a drug target. *Trends Pharmacol Sci.* 2009; 30(3): 105–111. Epub 2009/02/13. <https://doi.org/10.1016/j.tips.2008.11.006> PMID: 19211160.
28. Bonsi P, Ponterio G, Vanni V, Tassone A, Sciamanna G, Migliarini S, et al. RGS9-2 rescues dopamine D2 receptor levels and signaling in DYT1 dystonia mouse models. *EMBO Mol Med.* 2019; 11(1). <https://doi.org/10.15252/emmm.201809283> PMID: 30552094.
29. Seeman P, Schwarz J, Chen JF, Szechtman H, Perreault M, McKnight GS, et al. Psychosis pathways converge via D2high dopamine receptors. *Synapse.* 2006; 60(4): 319–346. <https://doi.org/10.1002/syn.20303> PMID: 16786561
30. Seeman P. All roads to schizophrenia lead to dopamine supersensitivity and elevated dopamine D2 (high) receptors. *CNS Neurosci Ther.* 2011; 17(2): 118–132. Epub 2010/06/22. <https://doi.org/10.1111/j.1755-5949.2010.00162.x> PMID: 20560996.
31. Maple AM, Perna MK, Parlaman JP, Stanwood GD, Brown RW. Ontogenetic quinpirole treatment produces long-lasting decreases in the expression of RGS9, but increases RGS17 in the striatum,

- nucleus accumbens and frontal cortex. *Eur J Neurosci.* 2007; 26(9): 2532–2538. Epub 2007/11/01. <https://doi.org/10.1111/j.1460-9568.2007.05860.x> PMID: 17970732.
32. Seeman P, Ko F, Jack E, Greenstein R, Dean B. Consistent with dopamine supersensitivity, RGS9 expression is diminished in the amphetamine-treated animal model of schizophrenia and in postmortem schizophrenia brain. *Synapse.* 2007; 61(5): 303–309. Epub 2007/02/24. <https://doi.org/10.1002/syn.20368> PMID: 17318883.
 33. Calabresi P, Pisani A, Rothwell J, Ghiglieri V, Obeso JA, Picconi B. Hyperkinetic disorders and loss of synaptic downscaling. *Nat Neurosci.* 2016; 19(7): 868–875. Epub 2016/06/29. <https://doi.org/10.1038/nn.4306> PMID: 27351172.
 34. Xie K, Martemyanov KA. Control of striatal signaling by g protein regulators. *Front Neuroanat.* 2011; 5: 49. Epub 2011/08/20. <https://doi.org/10.3389/fnana.2011.00049> PMID: 21852966.
 35. Gold SJ, Hoang CV, Potts BW, Porras G, Pioli E, Kim KW, et al. RGS9-2 negatively modulates L-3,4-dihydroxyphenylalanine-induced dyskinesia in experimental Parkinson's disease. *J Neurosci.* 2007; 27(52): 14338–14348. Epub 2007/12/28. <https://doi.org/10.1523/JNEUROSCI.4223-07.2007> PMID: 18160641.
 36. Dessauer CW, Tesmer JJ, Sprang SR, Gilman AG. Identification of a G α binding site on type V adenylyl cyclase. *J Biol Chem.* 1998; 273(40): 25831–25839. <https://doi.org/10.1074/jbc.273.40.25831> PMID: 9748257
 37. Hu B, Nakata H, Gu C, De Beer T, Cooper DM. A critical interplay between Ca²⁺ inhibition and activation by Mg²⁺ of AC5 revealed by mutants and chimeric constructs. *J Biol Chem.* 2002; 277(36): 33139–33147. <https://doi.org/10.1074/jbc.M112373200> PMID: 12065575.
 38. Bhalla US, Iyengar R. Emergent properties of networks of biological signaling pathways. *Science.* 1999; 283(5400): 381–387. <https://doi.org/10.1126/science.283.5400.381> PMID: 9888852.
 39. Urakubo H, Honda M, Tanaka K, Kuroda S. Experimental and computational aspects of signaling mechanisms of spike-timing-dependent plasticity. *HFSP J.* 2009; 3(4): 240–254. Epub 2010/02/02. <https://doi.org/10.2976/1.3137602> PMID: 20119481.
 40. Dupre DJ, Robitaille M, Rebois RV, Hebert TE. The role of G $\beta\gamma$ subunits in the organization, assembly, and function of GPCR signaling complexes. *Annu Rev Pharmacol Toxicol.* 2009; 49: 31–56. Epub 2008/10/07. <https://doi.org/10.1146/annurev-pharmtox-061008-103038> PMID: 18834311.
 41. Katanaev VL, Chornomoretz M. Kinetic diversity in G-protein-coupled receptor signalling. *Biochem J.* 2007; 401(2): 485–495. <https://doi.org/10.1042/BJ20060517> PMID: 16989639.
 42. Rice ME, Cragg SJ. Dopamine spillover after quantal release: rethinking dopamine transmission in the nigrostriatal pathway. *Brain Res Rev.* 2008; 58(2): 303–313. Epub 2008/04/25. <https://doi.org/10.1016/j.brainresrev.2008.02.004> PMID: 18433875.
 43. Patriarchi T, Cho JR, Merten K, Howe MW, Marley A, Xiong WH, et al. Ultrafast neuronal imaging of dopamine dynamics with designed genetically encoded sensors. *Science.* 2018; 360(6396). <https://doi.org/10.1126/science.aat4422> PMID: 29853555.
 44. Labouesse MA, Cola RB, Patriarchi T. GPCR-Based Dopamine Sensors-A Detailed Guide to Inform Sensor Choice for In vivo Imaging. *Int J Mol Sci.* 2020; 21(21). Epub 2020/11/01. <https://doi.org/10.3390/ijms21218048> PMID: 33126757.
 45. Beyene AG, McFarlane IR, Pinals RL, Landry MP. Stochastic Simulation of Dopamine Neuromodulation for Implementation of Fluorescent Neurochemical Probes in the Striatal Extracellular Space. *ACS Chem Neurosci.* 2017; 8(10): 2275–2289. Epub 2017/07/18. <https://doi.org/10.1021/acchemneuro.7b00193> PMID: 28714693.
 46. Hollinger S, Hepler JR. Cellular regulation of RGS proteins: modulators and integrators of G protein signaling. *Pharmacol Rev.* 2002; 54(3): 527–559. Epub 2002/09/12. <https://doi.org/10.1124/pr.54.3.527> PMID: 12223533.
 47. Levin LR, Reed RR. Identification of functional domains of adenylyl cyclase using in vivo chimeras. *J Biol Chem.* 1995; 270(13): 7573–7579. Epub 1995/03/31. <https://doi.org/10.1074/jbc.270.13.7573> PMID: 7706305.
 48. Hurley JH. Structure, mechanism, and regulation of mammalian adenylyl cyclase. *J Biol Chem.* 1999; 274(12): 7599–7602. Epub 1999/03/13. <https://doi.org/10.1074/jbc.274.12.7599> PMID: 10075642.
 49. Chen-Goodspeed M, Lukan AN, Dessauer CW. Modeling of G α_s and G α_i regulation of human type V and VI adenylyl cyclase. *J Biol Chem.* 2005; 280(3): 1808–1816. Epub 2004/11/17. <https://doi.org/10.1074/jbc.M409172200> PMID: 15545274.
 50. Anderson GR, Lujan R, Semenov A, Pravetoni M, Posokhova EN, Song JH, et al. Expression and localization of RGS9-2/G 5/R7BP complex in vivo is set by dynamic control of its constitutive degradation by cellular cysteine proteases. *J Neurosci.* 2007; 27(51): 14117–14127. Epub 2007/12/21. <https://doi.org/10.1523/JNEUROSCI.3884-07.2007> PMID: 18094251.

51. Araki KY, Sims JR, Bhide PG. Dopamine receptor mRNA and protein expression in the mouse corpus striatum and cerebral cortex during pre- and postnatal development. *Brain Res.* 2007; 1156: 31–45. Epub 2007/05/19. <https://doi.org/10.1016/j.brainres.2007.04.043> PMID: 17509542.
52. Seeman P. Dopamine receptors and the dopamine hypothesis of schizophrenia. *Synapse.* 1987; 1(2): 133–152. Epub 1987/01/01. <https://doi.org/10.1002/syn.890010203> PMID: 2905529.
53. Farde L, Nordstrom AL, Wiesel FA, Pauli S, Halldin C, Sedvall G. Positron emission tomographic analysis of central D1 and D2 dopamine receptor occupancy in patients treated with classical neuroleptics and clozapine. Relation to extrapyramidal side effects. *Arch Gen Psychiatry.* 1992; 49(7): 538–544. Epub 1992/07/01. <https://doi.org/10.1001/archpsyc.1992.01820070032005> PMID: 1352677.
54. Napolitano F, Pasqualetti M, Usiello A, Santini E, Pacini G, Sciamanna G, et al. Dopamine D2 receptor dysfunction is rescued by adenosine A2A receptor antagonism in a model of DYT1 dystonia. *Neurobiol Dis.* 2010; 38(3): 434–445. Epub 2010/03/17. <https://doi.org/10.1016/j.nbd.2010.03.003> PMID: 20227500.
55. Celver J, Sharma M, Kovoov A. D2-Dopamine receptors target regulator of G protein signaling 9–2 to detergent-resistant membrane fractions. *Journal of Neurochemistry.* 2012; 120(1): 56–69. WOS:000298060500007. <https://doi.org/10.1111/j.1471-4159.2011.07559.x> PMID: 22035199
56. Stephans SE, Yamamoto BK. Methamphetamine-induced neurotoxicity: roles for glutamate and dopamine efflux. *Synapse.* 1994; 17(3): 203–209. Epub 1994/07/01. <https://doi.org/10.1002/syn.890170310> PMID: 7974204.
57. Dong H, Wang J, Yang YF, Shen Y, Qu WM, Huang ZL. Dorsal Striatum Dopamine Levels Fluctuate Across the Sleep-Wake Cycle and Respond to Salient Stimuli in Mice. *Front Neurosci.* 2019; 13: 242. Epub 2019/04/06. <https://doi.org/10.3389/fnins.2019.00242> PMID: 30949023.
58. Hanoune J, Defer N. Regulation and role of adenylyl cyclase isoforms. *Annu Rev Pharmacol Toxicol.* 2001; 41: 145–174. Epub 2001/03/27. <https://doi.org/10.1146/annurev.pharmtox.41.1.145> PMID: 11264454.
59. Narzi D, van Keulen SC, Rothlisberger U. Gα1 inhibition mechanism of ATP-bound adenylyl cyclase type 5. *PLoS One.* 2021; 16(1): e0245197. Epub 2021/01/26. <https://doi.org/10.1371/journal.pone.0245197> PMID: 33493164.
60. Kesby JP, Eyles DW, McGrath JJ, Scott JG. Dopamine, psychosis and schizophrenia: the widening gap between basic and clinical neuroscience. *Transl Psychiatry.* 2018; 8(1): 30. Epub 2018/02/01. <https://doi.org/10.1038/s41398-017-0071-9> PMID: 29382821.
61. Kellendonk C, Simpson EH, Polan HJ, Malleret G, Vronskaya S, Winiger V, et al. Transient and selective overexpression of dopamine D2 receptors in the striatum causes persistent abnormalities in prefrontal cortex functioning. *Neuron.* 2006; 49(4): 603–615. Epub 2006/02/16. <https://doi.org/10.1016/j.neuron.2006.01.023> PMID: 16476668.
62. McCutcheon RA, Abi-Dargham A, Howes OD. Schizophrenia, Dopamine and the Striatum: From Biology to Symptoms. *Trends Neurosci.* 2019; 42(3): 205–220. Epub 2019/01/10. <https://doi.org/10.1016/j.tins.2018.12.004> PMID: 30621912.
63. Gold SJ, Ni YG, Dohlman HG, Nestler EJ. Regulators of G-protein signaling (RGS) proteins: Region-specific expression of nine subtypes in rat brain. *Journal of Neuroscience.* 1997; 17(20): 8024–8037. ISI:A1997XZ44900042. <https://doi.org/10.1523/JNEUROSCI.17-20-08024.1997> PMID: 9315921
64. Celver J, Sharma M, Kovoov A. RGS9-2 mediates specific inhibition of agonist-induced internalization of D2-dopamine receptors. *J Neurochem.* 2010; 114(3): 739–749. Epub 2010/05/19. <https://doi.org/10.1111/j.1471-4159.2010.06805.x> PMID: 20477943.
65. Kovoov A, Seyffarth P, Ebert J, Barghshoon S, Chen CK, Schwarz S, et al. D2 dopamine receptors colocalize regulator of G-protein signaling 9–2 (RGS9-2) via the RGS9 DEP domain, and RGS9 knock-out mice develop dyskinesias associated with dopamine pathways. *J Neurosci.* 2005; 25(8): 2157–2165. Epub 2005/02/25. <https://doi.org/10.1523/JNEUROSCI.2840-04.2005> PMID: 15728856.
66. Burns ME, Pugh EN Jr. Lessons from photoreceptors: turning off G-protein signaling in living cells. *Physiology (Bethesda).* 2010; 25(2): 72–84. <https://doi.org/10.1152/physiol.00001.2010> PMID: 20430952.
67. Korenbrot JL. Speed, sensitivity, and stability of the light response in rod and cone photoreceptors: facts and models. *Prog Retin Eye Res.* 2012; 31(5): 442–466. Epub 2012/06/05. <https://doi.org/10.1016/j.preteyeres.2012.05.002> PMID: 22658984.
68. Zhang X, Nagai T, Ahammad RU, Kuroda K, Nakamuta S, Nakano T, et al. Balance between dopamine and adenosine signals regulates the PKA/Rap1 pathway in striatal medium spiny neurons. *Neurochem Int.* 2019; 122: 8–18. <https://doi.org/10.1016/j.neuint.2018.10.008> PMID: 30336179.
69. Grafstein-Dunn E, Young KH, Cockett MI, Khawaja XZ. Regional distribution of regulators of G-protein signaling (RGS) 1, 2, 13, 14, 16, and GAIP messenger ribonucleic acids by in situ hybridization in rat

- brain. *Brain Res Mol Brain Res*. 2001; 88(1–2): 113–123. Epub 2001/04/11. [https://doi.org/10.1016/S0169-328X\(01\)00038-9](https://doi.org/10.1016/S0169-328X(01)00038-9) PMID: 11295237.
70. Rafelski SM, Marshall WF. Building the cell: design principles of cellular architecture. *Nat Rev Mol Cell Biol*. 2008; 9(8): 593–602. Epub 2008/07/24. <https://doi.org/10.1038/nrm2460> PMID: 18648373
 71. Cazorla M, de Carvalho FD, Chohan MO, Shegda M, Chuhma N, Rayport S, et al. Dopamine D2 receptors regulate the anatomical and functional balance of basal ganglia circuitry. *Neuron*. 2014; 81(1): 153–164. Epub 2014/01/15. <https://doi.org/10.1016/j.neuron.2013.10.041> PMID: 24411738.
 72. Lerner V, Miodownik C. Motor symptoms of schizophrenia: is tardive dyskinesia a symptom or side effect? A modern treatment. *Curr Psychiatry Rep*. 2011; 13(4): 295–304. Epub 2011/04/27. <https://doi.org/10.1007/s11920-011-0202-6> PMID: 21519907.
 73. Ribot B, Aupy J, Vidailhet M, Mazere J, Pisani A, Bezard E, et al. Dystonia and dopamine: From phenomenology to pathophysiology. *Prog Neurobiol*. 2019; 182: 101678. Epub 2019/08/14. <https://doi.org/10.1016/j.pneurobio.2019.101678> PMID: 31404592.
 74. D'Angelo V, Paldino E, Cardarelli S, Sorge R, Fusco FR, Biagioni S, et al. Dystonia: Sparse Synapses for D2 Receptors in Striatum of a DYT1 Knock-out Mouse Model. *Int J Mol Sci*. 2020; 21(3). Epub 2020/02/12. <https://doi.org/10.3390/ijms21031073> PMID: 32041188.
 75. Maltese M, Martella G, Madeo G, Fagiolo I, Tassone A, Ponterio G, et al. Anticholinergic drugs rescue synaptic plasticity in DYT1 dystonia: role of M1 muscarinic receptors. *Mov Disord*. 2014; 29(13): 1655–1665. Epub 2014/09/10. <https://doi.org/10.1002/mds.26009> PMID: 25195914.
 76. Martella G, Maltese M, Nistico R, Schirizzi T, Madeo G, Sciamanna G, et al. Regional specificity of synaptic plasticity deficits in a knock-in mouse model of DYT1 dystonia. *Neurobiol Dis*. 2014; 65: 124–132. Epub 2014/02/08. <https://doi.org/10.1016/j.nbd.2014.01.016> PMID: 24503369.
 77. Sciamanna G, Ponterio G, Vanni V, Laricchiuta D, Martella G, Bonsi P, et al. Optogenetic Activation of Striatopallidal Neurons Reveals Altered HCN Gating in DYT1 Dystonia. *Cell Rep*. 2020; 31(7): 107644. Epub 2020/05/21. <https://doi.org/10.1016/j.celrep.2020.107644> PMID: 32433955.
 78. Lerner RP, Niethammer M, Eidelberg D. Understanding the anatomy of dystonia: determinants of penetrance and phenotype. *Curr Neurol Neurosci Rep*. 2013; 13(11): 401. Epub 2013/10/12. <https://doi.org/10.1007/s11910-013-0401-0> PMID: 24114145.
 79. Albanese A, Bhatia K, Bressman SB, Delong MR, Fahn S, Fung VS, et al. Phenomenology and classification of dystonia: a consensus update. *Mov Disord*. 2013; 28(7): 863–873. Epub 2013/05/08. <https://doi.org/10.1002/mds.25475> PMID: 23649720.
 80. Cloud LJ, Jinnah HA. Treatment strategies for dystonia. *Expert Opin Pharmacother*. 2010; 11(1): 5–15. Epub 2009/12/17. <https://doi.org/10.1517/14656560903426171> PMID: 20001425.
 81. Schizophrenia Working Group of the Psychiatric Genomics C. Biological insights from 108 schizophrenia-associated genetic loci. *Nature*. 2014; 511(7510): 421–427. Epub 2014/07/25. <https://doi.org/10.1038/nature13595> PMID: 25056061.
 82. Jenner P. Molecular mechanisms of L-DOPA-induced dyskinesia. *Nat Rev Neurosci*. 2008; 9(9): 665–677. Epub 2008/08/21. <https://doi.org/10.1038/nrn2471> PMID: 18714325.
 83. Fieblinger T, Graves SM, Sebel LE, Alcaccer C, Plotkin JL, Gertler TS, et al. Cell type-specific plasticity of striatal projection neurons in parkinsonism and L-DOPA-induced dyskinesia. *Nat Commun*. 2014; 5: 5316. Epub 2014/11/02. <https://doi.org/10.1038/ncomms6316> PMID: 25360704.
 84. Darmopil S, Martin AB, De Diego IR, Ares S, Moratalla R. Genetic inactivation of dopamine D1 but not D2 receptors inhibits L-DOPA-induced dyskinesia and histone activation. *Biol Psychiatry*. 2009; 66(6): 603–613. Epub 2009/06/13. <https://doi.org/10.1016/j.biopsych.2009.04.025> PMID: 19520364.
 85. Murer MG, Moratalla R. Striatal Signaling in L-DOPA-Induced Dyskinesia: Common Mechanisms Involving Drug Abuse and Long Term Memory Involving D1 Dopamine Receptor Stimulation. *Front Neuroanat*. 2011; 5: 51. Epub 2011/09/03. <https://doi.org/10.3389/fnana.2011.00051> PMID: 21886608.
 86. Ryan MB, Bair-Marshall C, Nelson AB. Aberrant Striatal Activity in Parkinsonism and Levodopa-Induced Dyskinesia. *Cell Rep*. 2018; 23(12): 3438–3446 e3435. Epub 2018/06/21. <https://doi.org/10.1016/j.celrep.2018.05.059> PMID: 29924988.
 87. Yarali A, Nehrkorn J, Tanimoto H, Herz AV. Event timing in associative learning: from biochemical reaction dynamics to behavioural observations. *PLoS One*. 2012; 7(3): e32885. <https://doi.org/10.1371/journal.pone.0032885> PMID: 22493657.
 88. Yovell Y, Abrams TW. Temporal asymmetry in activation of Aplysia adenyl cyclase by calcium and transmitter may explain temporal requirements of conditioning. *Proc Natl Acad Sci U S A*. 1992; 89(14): 6526–6530. <https://doi.org/10.1073/pnas.89.14.6526> PMID: 1631153.
 89. Abrams TW, Yovell Y, Onyike CU, Cohen JE, Jarrard HE. Analysis of sequence-dependent interactions between transient calcium and transmitter stimuli in activating adenyl cyclase in Aplysia:

- possible contribution to CS-US sequence requirement during conditioning. *Learning & Memory*. 1998; 4(6): 496–509. <https://doi.org/10.1101/lm.4.6.496> PMID: 10701874
90. Yovell Y, Kandel ER, Dudai Y, Abrams TW. A quantitative study of the Ca²⁺/calmodulin sensitivity of adenylyl cyclase in *Aplysia*, *Drosophila*, and rat. *J Neurochem*. 1992; 59(5): 1736–1744. <https://doi.org/10.1111/j.1471-4159.1992.tb11005.x> PMID: 1402918.
 91. Nair AG, Bhalla US, Hellgren Kotaleski J. Role of DARPP-32 and ARPP-21 in the Emergence of Temporal Constraints on Striatal Calcium and Dopamine Integration. *PLoS Comput Biol*. 2016; 12(9): e1005080. <https://doi.org/10.1371/journal.pcbi.1005080> PMID: 27584878.
 92. Matsuoka I, Suzuki Y, Defer N, Nakanishi H, Hanoune J. Differential expression of type I, II, and V adenylyl cyclase gene in the postnatal developing rat brain. *J Neurochem*. 1997; 68(2): 498–506. Epub 1997/02/01. <https://doi.org/10.1046/j.1471-4159.1997.68020498.x> PMID: 9003034.
 93. Lundblad M, Price DA, Burmeister JJ, Quintero JE, Huettl P, Pomerleau F, et al. Tonic and Phasic Amperometric Monitoring of Dopamine Using Microelectrode Arrays in Rat Striatum. *Appl Sci-Basel*. 2020; 10(18). WOS:000580423500001. <https://doi.org/10.3390/app10186187> PMID: 34306736
 94. Menegas W, Bergan JF, Ogawa SK, Isogai Y, Umadevi Venkataraju K, Osten P, et al. Dopamine neurons projecting to the posterior striatum form an anatomically distinct subclass. *Elife*. 2015; 4: e10032. Epub 2015/09/01. <https://doi.org/10.7554/eLife.10032> PMID: 26322384.
 95. Puig MV, Rose J, Schmidt R, Freund N. Dopamine modulation of learning and memory in the prefrontal cortex: insights from studies in primates, rodents, and birds. *Front Neural Circuits*. 2014; 8: 93. Epub 2014/08/21. <https://doi.org/10.3389/fncir.2014.00093> PMID: 25140130.
 96. Cechova S, Venton BJ. Transient adenosine efflux in the rat caudate-putamen. *J Neurochem*. 2008; 105(4): 1253–1263. Epub 2008/01/16. <https://doi.org/10.1111/j.1471-4159.2008.05223.x> PMID: 18194431.
 97. Nguyen MD, Lee ST, Ross AE, Ryals M, Choudhry VI, Venton BJ. Characterization of spontaneous, transient adenosine release in the caudate-putamen and prefrontal cortex. *PLoS One*. 2014; 9(1): e87165. Epub 2014/02/05. <https://doi.org/10.1371/journal.pone.0087165> PMID: 24494035.
 98. Ribeiro JA, Sebastiao AM, de Mendonca A. Adenosine receptors in the nervous system: pathophysiological implications. *Prog Neurobiol*. 2002; 68(6): 377–392. Epub 2003/02/11. [https://doi.org/10.1016/s0301-0082\(02\)00155-7](https://doi.org/10.1016/s0301-0082(02)00155-7) PMID: 12576292.
 99. Gomes CV, Kaster MP, Tome AR, Agostinho PM, Cunha RA. Adenosine receptors and brain diseases: neuroprotection and neurodegeneration. *Biochim Biophys Acta*. 2011; 1808(5): 1380–1399. Epub 2010/12/15. <https://doi.org/10.1016/j.bbame.2010.12.001> PMID: 21145878.
 100. Apicella P. Leading tonically active neurons of the striatum from reward detection to context recognition. *Trends in Neurosciences*. 2007; 30(6): 299–306. WOS:000247277800007. <https://doi.org/10.1016/j.tins.2007.03.011> PMID: 17420057
 101. Hersch SM, Gutekunst CA, Rees HD, Heilman CJ, Levey AI. Distribution of m1-m4 muscarinic receptor proteins in the rat striatum: light and electron microscopic immunocytochemistry using subtype-specific antibodies. *J Neurosci*. 1994; 14(5 Pt 2): 3351–3363. Epub 1994/05/01. <https://doi.org/10.1523/JNEUROSCI.14-05-03351.1994> PMID: 8182478.
 102. Chuhma N, Mingote S, Moore H, Rayport S. Dopamine neurons control striatal cholinergic neurons via regionally heterogeneous dopamine and glutamate signaling. *Neuron*. 2014; 81(4): 901–912. <https://doi.org/10.1016/j.neuron.2013.12.027> PMID: 24559678.
 103. Chuhma N, Mingote S, Yetnikoff L, Kalmbach A, Ma T, Ztaou S, et al. Dopamine neuron glutamate cotransmission evokes a delayed excitation in lateral dorsal striatal cholinergic interneurons. *Elife*. 2018; 7. Epub 2018/10/09. <https://doi.org/10.7554/eLife.39786> PMID: 30295607.
 104. Cai Y, Ford CP. Dopamine Cells Differentially Regulate Striatal Cholinergic Transmission across Regions through Corelease of Dopamine and Glutamate. *Cell Rep*. 2018; 25(11): 3148–3157 e3143. Epub 2018/12/13. <https://doi.org/10.1016/j.celrep.2018.11.053> PMID: 30540946.
 105. Cachope R, Cheer JF. Local control of striatal dopamine release. *Front Behav Neurosci*. 2014; 8: 188. Epub 2014/06/07. <https://doi.org/10.3389/fnbeh.2014.00188> PMID: 24904339.
 106. Kim T, Capps RA, Hamade KC, Barnett WH, Todorov DI, Latash EM, et al. The Functional Role of Striatal Cholinergic Interneurons in Reinforcement Learning From Computational Perspective. *Front Neural Circuits*. 2019; 13: 10. Epub 2019/03/09. <https://doi.org/10.3389/fncir.2019.00010> PMID: 30846930.
 107. Canals M, Marcellino D, Fanelli F, Ciruela F, de Benedetti P, Goldberg SR, et al. Adenosine A2A-dopamine D2 receptor-receptor heteromerization: qualitative and quantitative assessment by fluorescence and bioluminescence energy transfer. *J Biol Chem*. 2003; 278(47): 46741–46749. Epub 2003/08/23. <https://doi.org/10.1074/jbc.M306451200> PMID: 12933819.

108. Xie K, Masuho I, Shih CC, Cao Y, Sasaki K, Lai CW, et al. Stable G protein-effector complexes in striatal neurons: mechanism of assembly and role in neurotransmitter signaling. *Elife*. 2015; 4. Epub 2015/11/28. <https://doi.org/10.7554/eLife.10451> PMID: 26613416.
109. Navarro G, Cordini A, Casado-Anguera V, Moreno E, Cai NS, Cortes A, et al. Evidence for functional pre-coupled complexes of receptor heteromers and adenylyl cyclase. *Nat Commun*. 2018; 9(1): 1242. Epub 2018/03/30. <https://doi.org/10.1038/s41467-018-03522-3> PMID: 29593213.
110. Wreggett KA, De Lean A. The ternary complex model. Its properties and application to ligand interactions with the D2-dopamine receptor of the anterior pituitary gland. *Mol Pharmacol*. 1984; 26(2): 214–227. Epub 1984/09/01. PMID: 6237254.
111. Richfield EK, Penney JB, Young AB. Anatomical and affinity state comparisons between dopamine D1 and D2 receptors in the rat central nervous system. *Neuroscience*. 1989; 30(3): 767–777. Epub 1989/01/01. [https://doi.org/10.1016/0306-4522\(89\)90168-1](https://doi.org/10.1016/0306-4522(89)90168-1) PMID: 2528080.
112. Skinbjerg M, Sibley DR, Javitch JA, Abi-Dargham A. Imaging the high-affinity state of the dopamine D2 receptor in vivo: fact or fiction? *Biochem Pharmacol*. 2012; 83(2): 193–198. Epub 2011/09/29. <https://doi.org/10.1016/j.bcp.2011.09.008> PMID: 21945484.
113. Marcott PF, Mamaligas AA, Ford CP. Phasic dopamine release drives rapid activation of striatal D2-receptors. *Neuron*. 2014; 84(1): 164–176. <https://doi.org/10.1016/j.neuron.2014.08.058> PMID: 25242218.
114. Liu C, Goel P, Kaeser PS. Spatial and temporal scales of dopamine transmission. *Nat Rev Neurosci*. 2021; 22(6): 345–358. Epub 2021/04/11. <https://doi.org/10.1038/s41583-021-00455-7> PMID: 33837376.
115. Jiang D, Sibley DR. Regulation of D(1) dopamine receptors with mutations of protein kinase phosphorylation sites: attenuation of the rate of agonist-induced desensitization. *Mol Pharmacol*. 1999; 56(4): 675–683. PMID: 10496949.